NUMERICAL STUDY OF THE PLASMA TEARING INSTABILITY ON THE RESISTIVE TIME SCALE

FABRICE DELUZET[†], CLAUDIA NEGULESCU[†], MAURIZIO OTTAVIANI[*], STEFAN POSSANNER[†]

Abstract. In this work, a new numerical scheme for the reduced resistive MHD system (RMHD) is presented. Numerical simulations of RMHD are notoriously challenging because of the disparate time-scales, encompassing the Alfvén wave period and the resistive diffusion time, and because of the formation of thin internal layers, especially in the nonlinear phase. The new scheme is specifically designed for the study of the long time scale dynamics with large time steps. The key difficulty, namely the singularity of the system matrix in the limit of an infinite time scale disparity, is overcome by techniques inspired by asymptotic preserving (AP) methods. The reformulated version of the fully-implicit RMHD scheme is based on a 'micro-macro' (MM) scheme with a stabilization term. The tearing mode evolution and the formation of a magnetic island are considered as a test case. The advantages of the MM scheme with respect to standard implicit and explicit schemes are demonstrated. Good agreement with known analytical results in the regime of nonlinear growth and saturation of the magnetic island are obtained.

1. Introduction

The objective of this paper will be the study of the following singularly perturbed problem,

$$(P)_\varepsilon \quad \begin{cases} \partial_t \Delta\phi^\varepsilon + \{\phi^\varepsilon, \Delta\phi^\varepsilon\} = \dfrac{1}{\varepsilon}\{\psi^\varepsilon, \Delta\psi^\varepsilon\} + \Delta^2\phi^\varepsilon \\ \partial_t \psi^\varepsilon + \{\phi^\varepsilon, \psi^\varepsilon\} = \Delta\psi^\varepsilon - \Delta\psi_e\,, \end{cases} \tag{1.1}$$

defined on a domain $\Omega \subset \mathbb{R}_x \times \mathbb{R}_y$, where $\{\phi, \psi\} = \partial_x\phi\partial_y\psi - \partial_y\phi\partial_x\psi$ denotes the Poisson bracket. Special attention will be paid to its asymptotic behavior as the perturbation parameter ε tends to zero. In particular, we are interested in designing an efficient numerical scheme, based on asymptotic-preserving techniques, which will be able to solve $(P)_\varepsilon$ accurately, uniformly in ε.

The problem $(P)_\varepsilon$ provides the simplest setting for magnetic reconnection studies [6] in two space dimensions, where $(\phi^\varepsilon, \psi^\varepsilon)$ stand for the velocity stream function and the

Date: April 14, 2014.

Key words and phrases. Reduced MHD, Resistive plasma instabilities, Tearing modes, Singularly perturbed problem, Asymptotic-Preserving scheme.

poloidal flux function, respectively. It represents a scaled version of the reduced magneto-hydrodynamic model (RMHD), capable of describing the nonlinear evolution of the so-called resistive tearing instabilities [5], which are important phenomena in tokamak plasmas. It is known that these resistive MHD modes allow the formation of magnetic islands, which in turn may lead to disruptions. Disruptions are rapid terminations of a plasma discharge, with a violent release of thermal and magnetic energy. They pose a major problem to the design of tokamaks, as they can lead to the damage of the material components subject to strong mechanical stresses and to large particle and energy fluxes. A good understanding of the tearing mode instability is thus vital for improving the security and efficiency of tokamaks.

Tearing instabilities can be understood qualitatively to a certain extent by means of studying the eigenmodes [5] of the system (1.1). Linear [16] as well as non-linear theories [30] rely heavily on approximations and simplified geometries of the problem. Numerical simulations have been employed throughout the years to overcome the limitations of analytic theory, and to address more complex geometries often in the context of an application to a given device. In target applications for tokamak plasmas such as ITER the scaling parameter in $(P)_\varepsilon$ is of the order $\varepsilon \sim 10^{-16}$. This fact prohibits the use of explicit and semi-implicit schemes [17], due to ε-dependent restrictions on the time step such as stability conditions. Fully implicit schemes, used in several modern codes [9, 18, 21], have no stability time step limitations but suffer from a numerical singularity as $\varepsilon \to 0$. This means that the discretization matrix is singular in this limit, a reflection of the ill-posedness of the problem (1.1) when setting $\varepsilon = 0$. In this case a unique solution does not exist; one thus speaks of $(P)_\varepsilon$ as a singularly perturbed problem.

The time scale in the non-dimensional problem (1.1) is the resistive time scale, which is particularly suitable for studying the tearing instabilities. Fast plasma motions such as Alfvén waves have frequencies of the order $\varepsilon^{-1/2}$ in this scaling. It is important to note that the limit $\varepsilon \to 0$ in (1.1) is not the "ideal-MHD"-limit in which dissipation is eliminated from the RMHD system. Rather, it corresponds to a long-time limit ($t \to \infty$) performed *together with* the limit of vanishing dissipation, such that resistive effects like tearing instabilities are observed on time intervals of order one for all $\varepsilon \geq 0$. In other words, the smaller the resistivity in the system, the longer one looks in order to observe the resistive effects. The difference with the ideal-MHD limit will be discussed in more detail in the section "Physical Motivation and Modeling".

Over the past decade the numerical treatment of singularly perturbed problems has advanced significantly with the advent of asymptotic-preserving (AP) techniques [11,20,27]. AP schemes have an implicit part constructed to overcome the limitations of generic fully implicit and semi-implicit schemes, by assuring the correct asymptotic behavior when the small parameter tends to zero. They are designed to work accurately in both limits, when the parameter ε is of order unity or if it approaches zero. It is the aim of this paper to apply

such techniques to the RMHD problem (1.1). For this, a mathematical understanding of the singularly-perturbed problem is needed, in particular of its asymptotic behavior. The mathematical and hence also the numerical analysis of problem $(P)_\varepsilon$ is very arduous, due to several aspects, for example the disparity of time and space scales, represented by the small parameter ε, the occurrence of internal layers and also due to the nonlinear character of the system. Due to all these reasons the mathematical part of this work remains on a formal level, where some groundwork is achieved leading to a basic understanding and interpretation of the problem at hand. On the numerical side, we propose a scheme based on a reformulation of the original system which is equivalent to (1.1) for $\varepsilon > 0$ and which leads to a non-singular problem in the limit $\varepsilon \to 0$. A fully implicit discretization of the reformulated problem yields a numerical scheme capable of simulating tearing instabilities even for $\varepsilon = 0$.

The paper is organized as follows: In section 2 we present in detail the scaling which leads to (1.1) and we discuss the physical meaning of the limit $\varepsilon \to 0$. Moreover, a first outline of how to construct an AP scheme for the RMHD problem is given. Section 3 contains the mathematical part of this work. In section 4 we present the numerical schemes for solving the RMHD problem on the resistive time scale. In particular, we construct three auxiliary schemes, with the purpose of yielding reference solutions, and one scheme with AP characteristics, the so-called "micro-macro" scheme. Section 5 contains the numerical results, especially some studies of the tearing mode in the short-time as well as in the long-time regime. Simulation results obtained with the AP-like scheme regarding the growth of magnetic islands are compared to analytical results. Finally, we summarize and conclude the work in section 6.

2. Physical motivation and modeling

2.1. **Plasma dynamics in the framework of reduced MHD.** The basic single-fluid description of a quasi-neutral plasma is given by the MHD equations. To justify briefly the use of the problem $(P)_\varepsilon$ for the magnetic reconnection study, let us start from the incompressible, resistive MHD equations, describing the evolution of a plasma treated as an electrically conducting, incompressible fluid and given by

$$\begin{aligned} \partial_t \mathbf{v} + (\mathbf{v}\cdot\nabla)\mathbf{v} &= -\frac{1}{\rho_0}\nabla p + \frac{1}{\mu_0\rho_0}(\nabla\times\mathbf{B})\times\mathbf{B} + \nu\Delta\mathbf{v}\,, \\ \nabla\cdot\mathbf{v} &= 0\,, \\ \partial_t \mathbf{B} &= \nabla\times(\mathbf{v}\times\mathbf{B}) + \frac{\eta}{\mu_0}\Delta\mathbf{B}\,, \\ \nabla\cdot\mathbf{B} &= 0\,, \end{aligned} \tag{2.2}$$

where $\mathbf{v}$ is the plasma (ion) velocity, $\mathbf{B}$ the magnetic field and p the pressure determined by the incompressibility constraint $\nabla\cdot\mathbf{v} = 0$, which signifies also that the plasma density is

constant, $\rho_0 = const$, if initially constant. Moreover, μ_0 is the permeability of the vacuum, η the plasma resistivity and $\nu := \mu/\rho_0$ the kinematic viscosity (μ denoting the dynamic viscosity). It seems to be consistent from a physical point of view to impose the constraint of incompressibility, *i.e.* $\nabla \cdot \mathbf{v} = 0$, as we are interested in the description of resistive MHD modes, which grow slowly as compared to the transit time of sound waves.

To simplify this system, let us consider a situation with a dominant magnetic field $\mathbf{B}_0$, aligned with the z-direction, *i.e.* $\mathbf{B} = \mathbf{B}_p + B_0\mathbf{e}_z$, where the poloidal magnetic field $\mathbf{B}_p = (B_x, B_y, 0)$ satisfies $|\mathbf{B}_p| \ll |\mathbf{B}_0|$. This situation is rather realistic for tokamak plasmas, so that the plasma dynamics can be simply described by the reduced MHD system [5, 33]

$$(RMHD) \quad \begin{cases} \partial_t \Delta\phi + \{\phi, \Delta\phi\} = \dfrac{1}{\mu_0\rho_0}\{\psi, \Delta\psi\} + \nu\Delta^2\phi \\ \partial_t\psi + \{\phi, \psi\} = \dfrac{\eta}{\mu_0}(\Delta\psi - \Delta\psi_e)\,, \end{cases} \tag{2.3}$$

where the unknowns are now the poloidal velocity stream function $\phi : \Omega \times [0,T] \to \mathbb{R}$ and the poloidal flux function $\psi : \Omega \times [0,T] \to \mathbb{R}$. In this context Ω lies in the xy-plane and is referred to as the poloidal domain. Moreover, we recall that $\{\phi, \psi\} = \partial_x\phi\partial_y\psi - \partial_y\phi\partial_x\psi$ denotes the Poisson bracket and that the function $\psi_e : \Omega \to \mathbb{R}$ is a specified equilibrium. Furthermore, let $\mathbf{v}_p = (v_x, v_y, 0)$ stand for the poloidal plasma velocity. The stream and the flux functions are then related to the poloidal quantities $\mathbf{v}_p$ and $\mathbf{B}_p$ by the formulae

$$\mathbf{v}_p = \mathbf{e}_z \times \nabla\phi = \begin{pmatrix} -\partial_y\phi \\ \partial_x\phi \\ 0 \end{pmatrix}, \qquad \mathbf{B}_p = \mathbf{e}_z \times \nabla\psi = \begin{pmatrix} -\partial_y\psi \\ \partial_x\psi \\ 0 \end{pmatrix}. \tag{2.4}$$

It is clear that these relations guarantee divergence-free poloidal magnetic field (no magnetic monopoles) and incompressible poloidal motion, $\nabla \cdot \mathbf{v}_p = 0$. The isolines of ϕ, i.e. the curves defined by $\phi = const.$, are the streamlines of the plasma and the isolines of ψ are the magnetic field lines in the poloidal plane. Remark that the electric field $\mathbf{E}$ and the magnetic field $\mathbf{B}$ can be written in terms of an electrostatic potential χ and a vector potential $\mathbf{A}$,

$$\mathbf{E} = -\nabla\chi - \partial_t\mathbf{A}\,, \qquad \mathbf{B} = \nabla \times \mathbf{A}\,, \tag{2.5}$$

where in the RMHD limit one has the relations

$$\phi = \frac{\chi}{B_0}\,, \qquad \psi = -A_z\,. \tag{2.6}$$

The flux function can be identified as the negative z-component of the vector potential and the ion poloidal velocity $\mathbf{v}_p$ is approximated, in the asymptotic RMHD limit, by

$$\mathbf{v}_p = \frac{\mathbf{E} \times \mathbf{B}_0}{B_0^2}\,. \tag{2.7}$$

Frequently, the RMHD equations (2.3) are written in terms of the vorticity ω of the velocity field $\mathbf{v}_p$ and in terms of j_z, the z-component of the current density, defined by

$$\omega := \Delta\phi = \mathbf{e}_z \cdot (\nabla \times \mathbf{v}_p)\,, \qquad j_z := \Delta\psi = \mathbf{e}_z \cdot (\nabla \times \mathbf{B}_p)\,. \tag{2.8}$$

With these notations, the RMHD equations have the form

$$\begin{cases} \partial_t \omega + \mathbf{v}_p \cdot \nabla\omega = \dfrac{1}{\mu_0\rho_0}\mathbf{B}_p \cdot \nabla j_z + \nu\Delta\omega \\ \partial_t \psi + \mathbf{v}_p \cdot \nabla\psi = \dfrac{\eta}{\mu_0}(j_z - j_{z,e})\,. \end{cases} \tag{2.9}$$

Setting $\nu = \eta = 0$ in equation (2.3) resp. (2.9) yields the ideal RMHD equations.

2.2. **Non-dimensional RMHD system.** Let us present now a convenient normalization in order to write the resistive RMHD equations (2.3) in non-dimensional form. This procedure shall permit to identify some typical parameters, such as the magnetic Reynolds number $\mathcal{R}_m$ and the Lundquist number S_L, whose order of magnitude characterizes the different plasma regimes considered in this work.

Since the important plasma dynamics occurs in the poloidal plane, we normalize the magnetic field to a typical poloidal field $\bar{B}_p$. Moreover, we shall set a typical poloidal length scale $\bar{L}$ as well as a time scale $\bar{t}$, both related to the physical phenomena one wants to describe. Starting from this triplet $(\bar{B}_p, \bar{L}, \bar{t})$, the scale of the other quantities follow immediately

$$\bar{v} := \frac{\bar{L}}{\bar{t}}\,, \quad \bar{\phi} := \bar{v}\bar{L}\,, \quad \bar{\psi} := \bar{B}_p\bar{L}\,. \tag{2.10}$$

Replacing now in system (2.3) each quantity, for example ϕ, by $\phi = \bar{\phi}\,\phi'$, yields

$$\begin{cases} \partial_{t'}\Delta\phi' + \{\phi', \Delta\phi'\} = \dfrac{\bar{\psi}^2\bar{t}}{\mu_0\bar{L}^2\bar{\phi}\rho_0}\{\psi', \Delta\psi'\} + \dfrac{\nu\bar{t}}{\bar{L}^2}\Delta^2\phi' \\ \partial_{t'}\psi' + \{\phi', \psi'\} = \dfrac{\eta\bar{t}}{\mu_0\bar{L}^2}(\Delta\psi' - \Delta\psi'_e)\,. \end{cases} \tag{2.11}$$

Let us now introduce the Alfvén speed and the Alfvén time scale corresponding to the characteristic poloidal magnetic field strength,

$$v_A^2 := \frac{\bar{B}_p^2}{\mu_0\rho_0} = \frac{\bar{\psi}^2}{\mu_0\bar{L}^2\rho_0}\,, \quad \tau_A := \frac{\bar{L}^2\sqrt{\mu_0\rho_0}}{\bar{\psi}}\,, \tag{2.12}$$

the resistive speed and corresponding resistive time scale

$$v_\eta := \frac{\eta}{\mu_0\bar{L}}\,, \quad \tau_\eta := \frac{\mu_0\bar{L}^2}{\eta}\,, \tag{2.13}$$

as well as the magnetic Reynolds and Lundquist numbers

$$\mathcal{R}_m := \frac{\bar{L}v_A}{\nu}\,, \quad S_L := \frac{\mu_0\bar{L}v_A}{\eta}\,. \tag{2.14}$$

With these new definitions, system (2.11) writes

$$\begin{cases} \partial_{t'}\Delta\phi' + \{\phi', \Delta\phi'\} = \dfrac{v_A^2}{\bar{v}^2}\{\psi', \Delta\psi'\} + \dfrac{1}{\mathcal{R}_m}\dfrac{v_A}{\bar{v}}\Delta^2\phi' \\ \partial_{t'}\psi' + \{\phi', \psi'\} = \dfrac{1}{S_L}\dfrac{v_A}{\bar{v}}(\Delta\psi' - \Delta\psi'_e)\,. \end{cases} \tag{2.15}$$

In the following, we shall assume that

$$\mathcal{R}_m = S_L = 1/\sqrt{\varepsilon}\,, \tag{2.16}$$

with $\varepsilon \ll 1$ a small parameter. The assumption (2.16) signifies that the plasma dynamics we are interested in are characterized by very large magnetic Reynolds numbers as well as Lundquist numbers, which is a standard situation in tokamak plasmas. Moreover this ordering tells us that, via Eq. (2.14),

$$\frac{v_\eta}{v_A} = \sqrt{\varepsilon}\,, \qquad \frac{\tau_\eta}{\tau_A} = \frac{1}{\sqrt{\varepsilon}}\,, \tag{2.17}$$

which suggests that the reconnection process is slow compared to the Alfvén time scale. Two different regimes will be identified in the next subsection.

2.3. **RMHD time scales and aim of the present paper.** Let us assume that one is interested in describing phenomena arising on the Alfvén time scale. In this context, one has to choose for the typical time scale $\bar{t} = \tau_A$, yielding for fixed length scale $\bar{L}$ the characteristic velocity $\bar{v} = v_A$. The RMHD-model (2.15)-(2.17) normalized to the Alfvén time scale now reads

$$(RMHD)_A \begin{cases} \partial_{t'}\Delta\phi_A + \{\phi_A, \Delta\phi_A\} = \{\psi_A, \Delta\psi_A\} + \sqrt{\varepsilon}\Delta^2\phi_A \\ \partial_{t'}\psi_A + \{\phi_A, \psi_A\} = \sqrt{\varepsilon}(\Delta\psi_A - \Delta\psi_{e,A})\,, \qquad t' \in (0, T_A)\,. \end{cases} \tag{2.18}$$

Suitable initial and boundary conditions are to be defined later. If however, one is interested in describing phenomena arising on the resistive time scale, as we shall do in the present paper, one has to choose $\bar{t} = \tau_\eta$ and hence $\bar{v} = v_\eta$ for fixed length scale $\bar{L}$. This scaling yields the RMHD-model (2.15)-(2.17) on the resistive time scale:

$$(RMHD)_\eta \begin{cases} \partial_t\Delta\phi^\varepsilon + \{\phi^\varepsilon, \Delta\phi^\varepsilon\} = \dfrac{1}{\varepsilon}\{\psi^\varepsilon, \Delta\psi^\varepsilon\} + \Delta^2\phi^\varepsilon \\ \partial_t\psi^\varepsilon + \{\phi^\varepsilon, \psi^\varepsilon\} = \Delta\psi^\varepsilon - \Delta\psi_e\,, \qquad t \in (0, T)\,. \end{cases} \tag{2.19}$$

Remark that between the two scalings, one has the relations

$$t = \sqrt{\varepsilon}t'\,, \qquad \phi^\varepsilon = \frac{\phi_A}{\sqrt{\varepsilon}}\,, \qquad \psi^\varepsilon = \psi_A\,. \tag{2.20}$$

These relations (2.20) indicate that (2.19) is suitable for studying the evolution of (ϕ_A, ψ_A) given by (2.18) in the long-time limit, i.e. on the time scale where dissipation is important. Intuitively, passing to the resistive time variable t and leaving the length scale $\bar{L}$ unchanged

corresponds to 'pressing the fast-forward button' in the dynamics (2.18). Since ϕ is related to a typical velocity via (2.4), it is rescaled accordingly. The primary goal of our resistive scaling (2.19) is hence to focus on the nonlinear dynamics, in other words it permits us to follow the resistive effects in order to understand the magnetic reconnection process, rather than to follow the (linear) Alfvén-wave dynamics.

For $\varepsilon > 0$ the two scalings (2.18) and (2.19) are indeed completely equivalent on the continuous level. However, the dissimilarity between the Alfvén and the resistive scaling becomes apparent in the limit $\varepsilon \to 0$. Setting formally $\varepsilon = 0$ in (2.18) yields the ideal RMHD system, whereas putting $\varepsilon = 0$ in (2.19) leads to the completely different reduced model

$$(R) \begin{cases} \{\psi^0, \Delta\psi^0\} = 0 \\ \\ \partial_t \psi^0 + \{\phi^0, \psi^0\} = \Delta\psi^0 - \Delta\psi_e \,. \end{cases} \tag{2.21}$$

The difference between these two $\varepsilon \to 0$ limits can be understood from the following remark: On the Alfvén time scale, dissipation is gradually eliminated from the dynamics as $\varepsilon \to 0$, which means $\tau_\eta \to \infty$ or equivalently $v_\eta \to 0$. By contrast, on the resistive time scale one has dissipation due to the term $\Delta\psi^\varepsilon$ even for $\varepsilon = 0$. In this case, $\varepsilon \to 0$ corresponds to the limit of infinite poloidal magnetic field strength, or $v_A \to \infty$, equivalent to $\tau_A \to 0$. This limit $\varepsilon \to 0$ in Eq. (2.19) will be denoted as the *high-poloidal-field limit* (HPF-limit). It is of central interest in this work. On the Alfvén time scale the HPF-limit corresponds to

$$\varepsilon \to 0 \qquad \text{and} \qquad \sqrt{\varepsilon}\, T_A = const. \,, \tag{2.22}$$

which stands for vanishing dissipation *and* increasingly long times. From a numerical point of view it is clear that the HPF-limit (2.22) poses a challenge for existing semi- and fully-implicit, Alfvén-time-scaled RMHD schemes [9, 17, 18, 21], since the simulation times T_A tend to infinity as $\varepsilon \to 0$. In this work, we shall thus propose some numerical approximations of Eq. (2.19), i.e. RMHD on the resistive time scale, which we construct in such a way to yield good approximations even in the HPF-limit $\varepsilon \to 0$, at affordable computational cost.

The numerical resolution of the RMHD-model on the resistive time scale (2.19) is by no means a simple task, as this system represents a singularly perturbed problem. The main difficulty in its numerical resolution arises consequently for small $\varepsilon \ll 1$, due to the fact that the reduced model (2.21) is ill-posed. Formally, this can be noticed by remarking that for each solution (ψ^0, ϕ^0) of (2.21), the functions $(\psi^0, \phi^0 + \overline{\phi})$ constitute also a solution, for all $\overline{\phi}$ belonging to the kernel of $\{\cdot, \psi^0\}$, that means for each $\overline{\phi}$ being constant along the contour lines of ψ^0 (see section 3). The ill-posedness comes thus from the impossibility (in the limit $\varepsilon \to 0$) to determine ϕ^0 on the isolines of ψ^0, which are nothing else than the magnetic field lines, moving and reconnecting in the domain. One possibility to render

(2.21) well-posed is thus to find a way to set the value of ϕ^0 on the isolines of ψ^0, however this has to be done in accordance with the behaviour of the solution $(\psi^\varepsilon, \phi^\varepsilon)$ of problem (2.19) for small $\varepsilon \ll 1$.

Briefly, in order to be able to construct an efficient scheme, capable to solve (2.19) accurately, uniformly in ε, one has to try to answer the following questions:

(1) Does the sequence of solutions $\{(\phi^\varepsilon, \psi^\varepsilon)\}_{\varepsilon>0}$ of (2.19) converge for $\varepsilon \to 0$ towards a certain limit solution (ϕ^0, ψ^0), and in which sense?
(2) Can one identify the limit problem, i.e. the system of equations that is satisfied by (ϕ^0, ψ^0), and is this limit-model well-posed?
(3) Concerning the numerical part, is it possible to find a discretization of (2.19) that yields for $\varepsilon \to 0$ a consistent and stable discretization of the limit problem ?

The answer to these questions is far from being obvious, due to the nonlinearity of the problem as well as to the occurrence of internal layers in the problem as $\varepsilon \to 0$. The authors are still working on a rigorous mathematical treatment of these difficulties. In Section 3 we will give however some first mathematical insights in the behavior of the resistive RMHD problem (2.19), which shall be helpful for the construction of the first efficient scheme presented in Sections 4 and 5.

3. Mathematical groundwork

From now on we will be concerned with the study of the RMHD problem on the resistive time scale, denoted in the following by $(P)_\varepsilon$ and recalled here for clarity reasons,

$$(P)_\varepsilon \quad \begin{cases} \partial_t \Delta\phi^\varepsilon + \{\phi^\varepsilon, \Delta\phi^\varepsilon\} = \dfrac{1}{\varepsilon}\{\psi^\varepsilon, \Delta\psi^\varepsilon\} + \Delta^2\phi^\varepsilon \\ \partial_t \psi^\varepsilon + \{\phi^\varepsilon, \psi^\varepsilon\} = \Delta\psi^\varepsilon - \Delta\psi_e\,, \quad t \in (0,T)\,. \end{cases} \tag{3.23}$$

The purpose of this section is to exhibit the properties of the dominant operator appearing in (3.23), with the aim to shape up a Micro-Macro decomposition [14]. This decomposition yields a reformulated set of equations in which the limit $\varepsilon \to 0$ is transformed into a regular limit.

3.1. Study of the dominant operator.

First, some useful properties of the Poisson brackets are recalled. For any functions $\phi, \psi \in H^1(\mathbb{R}^2)$ the Poisson bracket is defined by

$$\{\phi, \psi\} := \partial_x\phi\,\partial_y\psi - \partial_x\psi\,\partial_y\phi\,. \tag{3.24}$$

We have the following properties:

(1) For any $\phi, \psi : \mathbb{R}^2 \to \mathbb{R}$,
$$\{\phi, \psi\} = -\{\psi, \phi\}\,. \tag{3.25}$$
(2) For any $\phi : \mathbb{R}^2 \to \mathbb{R}$ and smooth $j : \mathbb{R} \to \mathbb{R}$,
$$\{\phi, j(\phi)\} = 0. \tag{3.26}$$

(3) For smooth $\phi, \psi, \chi : \mathbb{R}^2 \to \mathbb{R}$ which are L_x- resp. L_y-periodic in x resp. y, one has

$$\int_\Omega \{\phi, \psi\}\chi \, dxdy = \int_\Omega \{\chi, \phi\}\psi \, dxdy = \int_\Omega \{\psi, \chi\}\phi \, dxdy \,, \tag{3.27}$$

where $\Omega = (0, L_x) \times (0, L_y)$. This is demonstrated thanks to integration by parts.

Let us denote in the following by $X_\sharp$ the subspace of the Banach-space X, consisting of those functions which are L_x- resp. L_y-periodic in x resp. y. For any fixed $\psi \in W^{2,\infty}_\sharp(\Omega)$, with $\Omega := (0, L_x) \times (0, L_y)$, we now introduce the following linear operator

$$T_\psi : \mathcal{D}_\sharp \subset L^2_\sharp(\Omega) \to L^2_\sharp(\Omega) \,, \qquad T_\psi(\cdot) := \{\psi, \cdot\} \,, \tag{3.28}$$

with the domain

$$\mathcal{D}_\sharp := \{\phi \in L^2_\sharp(\Omega) \ / \ \{\psi, \phi\} \in L^2_\sharp(\Omega)\} \,.$$

This operator T_ψ is the dominant transport operator in our singularly-perturbed problem (2.19), and has to be studied in more detail in order to understand the asymptotic behavior of the solutions to (3.23) as $\varepsilon \to 0$, and thus to be able to construct an efficient numerical scheme.

Let us remark here that, for fixed $\psi \in W^{2,\infty}_\sharp(\Omega)$, the magnetic field $\mathbf{B}_p = (-\partial_y\psi, \partial_x\psi, 0)^t$ is sufficiently smooth for our purposes and verifies $\nabla \cdot \mathbf{B}_p = 0$. With this notation, the operator T_ψ can be rewritten as

$$T_\psi(\phi) = \mathbf{B}_p \cdot \nabla\phi = \nabla \cdot (\mathbf{B}_p \, \phi) \,,$$

which can be helpful for its geometrical interpretation. Notice also that the domain $\mathcal{D}_\sharp$ can be equivalently rewritten as

$$\mathcal{D}_\sharp := \{\phi \in L^2_\sharp(\Omega) \ / \ \nabla \cdot (\mathbf{B}_p \, \phi) = \mathbf{B}_p \cdot \nabla\phi \in L^2_\sharp(\Omega)\} \,.$$

The kernel of T_ψ is given by

$$\mathcal{G}_\psi := \{g \in \mathcal{D}_\sharp \ / \ \{\psi, g\} = \mathbf{B}_p \cdot \nabla g = 0\} \,, \tag{3.29}$$

which corresponds to the set of functions which are constant along the field lines of $\mathbf{B}_p$, in other words constant along the level sets of ψ.

Defining the $L^2_\sharp$-orthogonal space to $\mathcal{G}_\psi$, as

$$\tilde{\mathcal{A}}_\psi := \{f \in L^2_\sharp(\Omega) \ / \ \int_\Omega gf \, dx = 0, \ \forall g \in \mathcal{G}_\psi\} = \mathcal{G}_\psi^\perp \,, \tag{3.30}$$

one has the unique decomposition (orthogonal projection theorem)

$$L^2_\sharp(\Omega) = \mathcal{G}_\psi \oplus^\perp \tilde{\mathcal{A}}_\psi \,, \tag{3.31}$$

which extends to

$$\mathcal{D}_\sharp = \mathcal{G}_\psi \oplus \mathcal{A}_\psi\,, \quad \mathcal{A}_\psi := \{f \in \mathcal{D}_\sharp \;/\; \int_\Omega g f\, dx = 0,\ \forall g \in \mathcal{G}_\psi\}\,. \tag{3.32}$$

Each function $\phi \in \mathcal{D}_\sharp$ can be hence uniquely decomposed as follows,

$$\phi = \overline{\phi} + \phi^\star\,, \qquad \overline{\phi} \in \mathcal{G}_\psi\,, \quad \phi^\star \in \mathcal{A}_\psi\,. \tag{3.33}$$

To visualize better this abstract framework, it is shown in Appendix A that this decomposition can be interpreted as the splitting of ϕ into its average value along the field lines of $\mathbf{B}_p$, *i.e.* $\overline{\phi} \in \mathcal{G}_\psi$ (with zero $\mathcal{G}$radient along the field lines), and its fluctuation part $\phi^\star \in \mathcal{A}_\psi$ (with zero $\mathcal{A}$verage along the field lines). The authors used in former works [12, 13] this decomposition for the design of some AP-schemes in the framework of anisotropic elliptic equations.

With the above definitions, we can now prove that the operator T_ψ is a one-to-one mapping between the following spaces

$$T_\psi : \mathcal{A}_\psi \to \tilde{\mathcal{A}}_\psi\,. \tag{3.34}$$

In other words, the problem

$$T_\psi(\phi) = f\,, \tag{3.35}$$

is uniquely solvable (in $\mathcal{A}_\psi$) if and only if $f \in \tilde{\mathcal{A}}_\psi$. Indeed, the uniqueness in $\mathcal{A}_\psi$ is immediate due to the $L^2_\sharp$-orthogonality of $\mathcal{A}_\psi$ and $\mathcal{G}_\psi$. Moreover, due to the properties of the Poisson bracket (3.27), one sees immediately that $\mathcal{I}m(T_\psi) \subset \tilde{\mathcal{A}}_\psi$. To prove the equality of these two subspaces, one remarks that any $f \in \tilde{\mathcal{A}}_\psi$, which is orthogonal to $\mathcal{I}m(T_\psi)$, *i.e.* satisfying $\int_\Omega f\,\xi dx = 0$ for all $\xi \in \mathcal{I}m(T_\psi)$, is equal to zero, $f \equiv 0$. This permits to show that $\overline{\mathcal{I}m(T_\psi)} = \tilde{\mathcal{A}}_\psi$. And as the image is a closed space, we conclude.

3.2. **Micro-Macro decomposition and reformulation of the problem.** Let us now propose a reformulation of (3.23), designed specifically for numerical simulations for small $\varepsilon \ll 1$. This reformulation relies on the assumption that $T_{\psi^\varepsilon}(\Delta\psi^\varepsilon)$ tends to zero in the whole domain as ε tends to zero, *i.e.*

$$\lim_{\varepsilon\to 0} \{\psi^\varepsilon(t,x,y), \Delta\psi^\varepsilon(t,x,y)\} = 0 \qquad \forall\, t > 0\,,\ f.a.a.\,(x,y) \in \Omega_p\,. \tag{3.36}$$

The numerical simulations[1] performed in section 5 indicate indeed that $\max_t ||\{\psi^\varepsilon, \Delta\psi^\varepsilon\}||_\infty \sim \varepsilon^{1/6}$.

[1]This behavior is obtained with the implicit reference scheme $(\mathrm{IMP})_\varepsilon$, introduced in section 4, for the range of values $10^{-10} \le \varepsilon \le 10^{-5}$.

Capitalizing on the property (3.36), we may reformulate the problem (3.23) by decomposing the current density $\Delta\psi^\varepsilon(t)$ as follows,

$$\Delta\psi^\varepsilon(t) = p^\varepsilon(t) + \varepsilon\theta^\varepsilon(t)\,, \quad p^\varepsilon(t) \in \mathcal{G}_{\psi^\varepsilon}\,, \quad \theta^\varepsilon(t) \in \mathcal{D}_\sharp\,. \tag{3.37}$$

The function $p^\varepsilon(t)$, called "macroscopic" part of the current density, belongs to the kernel of the dominant operator $\mathcal{T}_{\psi^\varepsilon}(\cdot)$ and is thus constant along the poloidal magnetic field lines. The function $\theta^\varepsilon(t)$ is called "microscopic" part, due to the factor ε in (3.37). Therefore, this decomposition is referred to as "Micro-Macro" decomposition.

We highlight that, for a given $\Delta\psi^\varepsilon(t)$, the decomposition (3.37) is not unique; it signifies only that the function $\theta^\varepsilon(t) \in \mathcal{D}_\sharp$ is one of the solutions of the problem

$$\{\psi^\varepsilon, \theta^\varepsilon\} = \frac{1}{\varepsilon}\{\psi^\varepsilon, \Delta\psi^\varepsilon\}\,.$$

This problem is uniquely solvable only if the part $\overline{\theta}^\varepsilon \in \mathcal{G}_{\psi^\varepsilon}$ of θ^ε is fixed (as explained in Section 3.1, see Eq. (3.35)), in other words if one prescribes the value of $\theta^\varepsilon(t)$ on the level sets of $\psi^\varepsilon(t)$. One manner to do this is to set $\overline{\theta}^\varepsilon \equiv 0$, which implies that the decomposition (3.37) is nothing else than the decomposition $\mathcal{D}_\sharp = \mathcal{G}_\psi \oplus \mathcal{A}_\psi$, the macroscopic part $p^\varepsilon(t) \in \mathcal{G}_{\psi^\varepsilon}$ being the mean value along the magnetic field lines, and the microscopic part $\varepsilon\theta^\varepsilon(t) \in \mathcal{A}_{\psi^\varepsilon}$ corresponding to the fluctuations. This procedure leads to the reformulation

$$(RF1)_\varepsilon \quad \begin{cases} \partial_t\Delta\phi^\varepsilon + \{\phi^\varepsilon, \Delta\phi^\varepsilon\} = \{\psi^\varepsilon, \theta^\varepsilon\} + \Delta^2\phi^\varepsilon \\ \partial_t\psi^\varepsilon + \{\phi^\varepsilon, \psi^\varepsilon\} = \Delta\psi^\varepsilon - \Delta\psi_e \\ \{\psi^\varepsilon, \Delta\psi^\varepsilon\} = \varepsilon\{\psi^\varepsilon, \theta^\varepsilon\} - \overline{\theta}^\varepsilon\,. \end{cases} \tag{3.38}$$

The introduction of the auxiliary variable $\theta^\varepsilon : I \times \Omega_p \to \mathbb{R}$ permits to isolate the macroscopic scale of the problem in the last equation of (3.38). The first equation of (3.38) contains the microscopic information that is lost in (P^ε) when the HPF-limit is investigated. This auxiliary unknown θ^ε can be also seen as a Lagrange multiplier corresponding to the constraint $\{\psi^\varepsilon, \Delta\psi^\varepsilon\} = 0$ in the limit $\varepsilon \to 0$.

Obviously, the reformulation (3.38) is completely equivalent to the original system of equations $(P)_\varepsilon$. Indeed, since we have $\{\psi^\varepsilon, g\} \in \tilde{\mathcal{A}}_{\psi^\varepsilon}$ for any $g \in \mathcal{D}_\sharp$, projecting the third equation of (3.38) onto $\mathcal{G}_{\psi^\varepsilon}$ and $\tilde{\mathcal{A}}_{\psi^\varepsilon}$, respectively, yields

$$\overline{\theta}^\varepsilon = 0\,, \qquad \{\psi^\varepsilon, \Delta\psi^\varepsilon\} = \varepsilon\{\psi^\varepsilon, \theta^\varepsilon\} \qquad \forall\varepsilon \geq 0\,, \tag{3.39}$$

which means that the additional term $\overline{\theta}^\varepsilon$ does not interfere with the Poisson brackets and secondly that $\overline{\theta}^\varepsilon \equiv 0$.

The advantage of the reformulation (3.38) as compared to $(P)_\varepsilon$ is however that in the limit $\varepsilon \to 0$, one gets

$$(P)_0 \quad \begin{cases} \partial_t \Delta\phi^0 + \{\phi^0, \Delta\phi^0\} = \{\psi^0, \theta^0\} + \Delta^2\phi^0 \\ \partial_t \psi^0 + \{\phi^0, \psi^0\} = \Delta\psi^0 - \Delta\psi_e \\ \{\psi^0, \Delta\psi^0\} + \overline{\theta}^0 = 0\,, \end{cases} \tag{3.40}$$

which is a well-posed problem, in contrast to (2.21). The Duality-Based scheme proposed in [12, 13] for an anisotropic elliptic problem is based on a similar kind of decomposition. We point out that a rigorous proof that the sequence of solutions $\{(\phi^\varepsilon, \psi^\varepsilon)\}_{\varepsilon>0}$ of (3.38) (and thus of (3.23)) converges to the solution (ϕ^0, ψ^0) of (3.40) has not yet been achieved. However, based on the formal equivalence of the systems for $\varepsilon > 0$ and on the results obtained in Section 5, the system (3.40) is conjectured to be the limit model: the set of well posed equations providing the limit of the solutions $(\phi^\varepsilon, \psi^\varepsilon)$.

It can be anticipated that the numerical discretization of the mean value $\overline{\theta}^\varepsilon$ along the magnetic field lines will be arduous. We shall show in the next section how to avoid this new difficulty by means of a second auxiliary variable, thus yielding a scheme which is easy to implement, even on space meshes that are not aligned with the field lines.

4. Numerical schemes for resistive RMHD

4.1. **Introductory remarks.** In this part we present several numerical schemes for the resolution of the RMHD problem on the resistive time scale (3.23). The presented schemes will be all based on finite difference approximations of the occurring derivatives. In subsection 4.2 the discretization parameters are introduced along with the space discretization matrices for the Laplace operator and for the linearized Poisson bracket. Subsection 4.3 contains two fully discrete "auxiliary" schemes, namely an Euler explicit and an Euler implicit scheme, respectively. Those schemes will provide, when possible, reference solutions for the RMHD problem, for which analytical solutions are not attainable. The core of this Section is subsection 4.4. It contains the here proposed new efficient numerical scheme, namely the "Micro-Macro" (MM) scheme, derived via the reformulated system (3.38).

Remark 4.1. ***(Perturbed equilibrium.)*** *Rather than solving for the pair $(\phi^\varepsilon, \psi^\varepsilon)$, i.e. the full stream function and the full flux function, solutions of Eq.* (3.23)*, we shall merely be interested in the perturbations of these quantities with respect to a specified equilibrium state (ϕ_e, ψ_e). The perturbations with respect to this equilibrium are then of the same order of magnitude, which is favorable for numerical computations. The equilibrium is chosen to be independent of time and of the parameter ε , in particular we shall specify in Section 5*

that $\phi_e \equiv 0$, $\psi_e = -\cos(x)$, *where we underline that the equilibrium flux function satisfies*

$$\{\psi_e, \Delta\psi_e\} = 0\,. \tag{4.41}$$

Defining now the perturbations by

$$\widetilde{\phi}^\varepsilon := \phi^\varepsilon - \phi_e = \phi^\varepsilon\,, \qquad \widetilde{\psi}^\varepsilon := \psi^\varepsilon - \psi_e\,, \tag{4.42}$$

and inserting these definitions into Eq. (3.23) yields the system

$$(\widetilde{P})_\varepsilon \begin{cases} \partial_t \Delta\widetilde{\phi}^\varepsilon + \{\widetilde{\phi}^\varepsilon, \Delta\widetilde{\phi}^\varepsilon\} = \dfrac{1}{\varepsilon}\left(\{\widetilde{\psi}^\varepsilon, \Delta\widetilde{\psi}^\varepsilon\} + \{\psi_e, \Delta\widetilde{\psi}^\varepsilon\} - \{\Delta\psi_e, \widetilde{\psi}^\varepsilon\}\right) + \Delta^2\widetilde{\phi}^\varepsilon \\ \partial_t\widetilde{\psi}^\varepsilon + \{\widetilde{\phi}^\varepsilon, \widetilde{\psi}^\varepsilon\} + \{\widetilde{\phi}^\varepsilon, \psi_e\} = \Delta\widetilde{\psi}^\varepsilon\,, \qquad t \in (0,T)\,, \end{cases} \tag{4.43}$$

which is to be solved for $(\widetilde{\phi}^\varepsilon, \widetilde{\psi}^\varepsilon)$. We remark that the Poisson brackets have been written in a way so to distinguish between linear and nonlinear terms.
On the Alfvén time-scale, similar manipulations lead to

$$(\widetilde{P})_A \begin{cases} \partial_{t'} \Delta\widetilde{\phi}_A + \{\widetilde{\phi}_A, \Delta\widetilde{\phi}_A\} = \{\widetilde{\psi}_A, \Delta\widetilde{\psi}_A\} + \{\psi_e, \Delta\widetilde{\psi}_A\} - \{\Delta\psi_e, \widetilde{\psi}_A\} + \sqrt{\varepsilon}\Delta^2\widetilde{\phi}_A \\ \partial_{t'}\widetilde{\psi}_A + \{\widetilde{\phi}_A, \widetilde{\psi}_A\} + \{\widetilde{\phi}_A, \psi_e\} = \sqrt{\varepsilon}\Delta\widetilde{\psi}_A\,, \qquad t' \in (0,T_A)\,, \quad T_A = T/\sqrt{\varepsilon}\,. \end{cases} \tag{4.44}$$

Remark 4.2. ***(Nonlinear terms.)*** *An important aspect of the numerical solution of the RMHD system* (4.43) *is the treatment of the nonlinear terms, i.e. the three Poisson brackets* $\{\widetilde{\phi}^\varepsilon, \Delta\widetilde{\phi}^\varepsilon\}$, $\{\widetilde{\psi}^\varepsilon, \Delta\widetilde{\psi}^\varepsilon\}$ *and* $\{\widetilde{\phi}^\varepsilon, \widetilde{\psi}^\varepsilon\}$. *These terms play a crucial role in the long-time simulations performed in Section 5, as they prevent the solutions from exploding and lead to a saturation regime. There are several ways to treat the nonlinearities. In this work we shall use a fixed-point iteration. Details are presented in subsection 4.3.*

Remark 4.3. ***(Second-order time discretization.)*** *In order to achieve second-order accuracy in time, we use the diagonally-implicit Runge Kutta [8] (DIRK) method. The corresponding DIRK discretizations are presented in Appendix B. However, in this section we shall present only first-order time-discretizations, in order to better underline the features of the micro-macro scheme.*

4.2. **Discretization parameters.** In what follows we suppose that the domain is given by $\Omega_p = [-L_x/2, L_x/2] \times [-L_y/2, L_y/2]$ and that all considered functions are doubly periodic in x and in y. For a time interval $I = (0,T)$, $T > 0$, resp. $I_A = (0, T_A)$, $T_A := T/\sqrt{\varepsilon} > 0$, we define the homogeneous time-discretization with $N_t + 1$ points, $N_t \in \mathbb{N}$,

$$t^n := n\tau\,, \qquad \tau := \frac{T}{N_t}\,, \qquad \tau' := \frac{T_A}{N_t} = \frac{\tau}{\sqrt{\varepsilon}}\,, \qquad n = 0, \dots, N_t\,.$$

Further, let us put a uniform mesh on the domain Ω_p by defining the grid spacings as

$$h_x := \frac{L_x}{(N_x - 1)}\,,\ h_y := \frac{L_y}{(N_y - 1)}\,, \quad x_i = (i-1)h_x - L_x/2\,,\ y_j = (j-1)h_y - L_y/2\,, \tag{4.45}$$

where $i \in \{1, 2, \dots, N_x - 1\}$ resp. $j \in \{1, 2, \dots, N_y - 1\}$. For functions $a : I_{(A)} \times \Omega_p \to \mathbb{R}$, we shall denote the approximation of $a(t^n, x_i, y_j)$ (resp. of the function $a(t^n, \cdot, \cdot)$) by a^n_{ij} (resp. by a^n_h). In view of the periodicity of $a : I_{(A)} \times \Omega_p \to \mathbb{R}$, we put

$$a^n_{N_x,j} := a^n_{1j}\,, \qquad a^n_{i,N_y} := a^n_{i1}\,, \qquad \forall\, n, i, j\,. \tag{4.46}$$

Let us proceed with the discretization of the differential operators appearing in RMHD. The discrete Laplace operator evaluated at the point (x_i, y_j) is defined as

$$(\Delta a_h)_{ij} := \frac{1}{h_x^2}\left(a_{i+1j} - 2a_{ij} + a_{i-1j}\right) + \frac{1}{h_y^2}\left(a_{ij+1} - 2a_{ij} + a_{ij-1}\right)\,. \tag{4.47}$$

Let us furthermore adopt the Arakawa discretization [3] for the Poisson brackets (note that we use curly brackets for the continuous representation and square brackets for the discrete counterpart). This discretization exhibits good properties with regard to accuracy (second order in space), stability as well as conservation properties of physical quantities (mean energy, mean vorticity) as compared to standard methods for solving 2D advection problems. For two functions $a, b : \Omega_p \to \mathbb{R}$, the discrete version of the bracket $\{a, b\}$ evaluated at the point (x_i, y_j) is defined as

$$\begin{aligned}([a_h, b_h])_{ij} := \frac{1}{12 h_x h_y}\Big(&a_{i+1j}\mathcal{A}_{ij} + a_{i-1j}\mathcal{B}_{ij} + a_{ij+1}\mathcal{C}_{ij} + a_{ij-1}\mathcal{D}_{ij} \\ &+ a_{i+1j+1}\mathcal{E}_{ij} + a_{i-1j-1}\mathcal{F}_{ij} + a_{i-1j+1}\mathcal{G}_{ij} + a_{i+1j-1}\mathcal{H}_{ij}\Big)\,,\end{aligned} \tag{4.48}$$

where the coefficients read

$$\begin{aligned}
\mathcal{A}_{ij} &:= +b_{ij+1} - b_{ij-1} + b_{i+1j+1} - b_{i+1j-1}\,, & \mathcal{E}_{ij} &:= +b_{ij+1} - b_{i+1j}\,,\\
\mathcal{B}_{ij} &:= -b_{ij+1} + b_{ij-1} - b_{i-1j+1} + b_{i-1j-1}\,, & \mathcal{F}_{ij} &:= -b_{i-1j} + b_{ij-1}\,,\\
\mathcal{C}_{ij} &:= -b_{i+1j} + b_{i-1j} - b_{i+1j+1} + b_{i-1j+1}\,, & \mathcal{G}_{ij} &:= -b_{ij+1} + b_{i-1j}\,,\\
\mathcal{D}_{ij} &:= +b_{i+1j} - b_{i-1j} + b_{i+1j-1} - b_{i-1j-1}\,, & \mathcal{H}_{ij} &:= +b_{i+1j} - b_{ij-1}\,.
\end{aligned} \tag{4.49}$$

The brackets $\{\Delta a, b\}$ and $\{\{a, b\}, b\}$ (to be encountered later in the MM-scheme) are discretized accordingly.

4.3. **Auxiliary schemes.** For the sake of a more transparent writing, from here on we shall omit the ε-dependence as well as the tildes in the notation of the discrete (and semi-discrete) solutions of (4.43). Hence we mean in the following

$$(\widetilde{\phi}^{\varepsilon,n}_h, \widetilde{\psi}^{\varepsilon,n}_h) \equiv (\phi^n_h, \psi^n_h)\,. \tag{4.50}$$

Whenever it is necessary to distinguish between the full stream and flux functions and the mere perturbations with respect to equilibrium, we shall explicitly mention it. Otherwise, from here on we are concerned with the perturbations only.

As a first auxiliary scheme, representing a full discretization of (4.43) for the perturbations, we construct an *explicit Euler* scheme:

$$(\mathrm{EXP})_\varepsilon \quad \begin{cases} \Delta\phi_h^{n+1} = \Delta\phi_h^n + \dfrac{\tau}{\varepsilon}\Big([\psi_h^n, \Delta\psi_h^n] + [\psi_{e,h}, \Delta\psi_h^n] - [\Delta\psi_{e,h}, \psi_h^n]\Big) \\ \qquad\qquad - \tau[\phi_h^n, \Delta\phi_h^n] + \tau\Delta^2\phi_h^n\,, \\ \\ \psi_h^{n+1} = \psi_h^n - \tau[\phi_h^{n+1}, \psi_h^n] - \tau[\phi_h^{n+1}, \psi_{e,h}] + \tau\Delta\psi_h^n\,. \end{cases} \tag{4.51}$$

At each time-step n, we first solve for ϕ_h^{n+1} and then use this solution in the second equation to compute ψ_h^{n+1}.

Remark 4.4. *(**Uniqueness of** ϕ_h^{n+1}) Due to the doubly-periodic boundary conditions, the solution of the elliptic problem for ϕ_h^{n+1} in Eq. (4.51) is not unique for any $\varepsilon \geq 0$, but defined up to a constant. Therefore, we set the value of ϕ_h^{n+1} at one point in the domain, i.e. the point $(x = -L_x/2, y = -L_y/2)$ corresponding to $(i = 1, j = 1)$,*

$$\phi_{11}^{n+1} = 0\,, \qquad \forall n \in \{0, 1, \ldots, N_t\}\,. \tag{4.52}$$

This form of fixing ϕ_h^{n+1} is used in all of the schemes presented below, and is not inappropriate from a physical point of view, as ϕ is somehow linked to an electrostatic potential and we are interested only in its gradients.

We remark that the time step in the explicit scheme has to be proportional to ε, for numerical stability reasons. Therefore, using this explicit scheme for simulating resistive effects (long time effects) is hardly feasible for realistic Reynolds and Lundquist numbers ($\varepsilon \leq 10^{-14}$), respectively. However, for values $\varepsilon \geq 10^{-6}$ (i.e. Lundquist and Reynolds numbers smaller than 10^3), we shall be able to obtain viable reference solutions from the explicit scheme. For smaller values of ε one has to turn to implicit schemes, introduced now.

A *fully implicit Euler* discretization of Eq. (4.43) reads

$$(\mathrm{IMP})_\varepsilon \quad \begin{cases} \varepsilon(\mathbb{1} - \tau\Delta)\Delta\phi_h^{n+1,k+1} + \tau[\Delta\psi_h^{n+1,k+1}, \psi_h^{n+1,k} + \psi_{e,h}] - \dfrac{\tau}{2}[\psi_h^{n+1,k+1}, \Delta\psi_{e,h}] \\ \qquad\qquad = \varepsilon\Delta\phi_h^n - \varepsilon\tau[\phi_h^{n+1,k}, \Delta\phi_h^{n+1,k}] + \dfrac{\tau}{2}[\psi_h^{n+1,k}, \Delta\psi_{e,h}]\,, \\ \\ (\mathbb{1} - \tau\Delta)\psi_h^{n+1,k+1} + \tau[\phi_h^{n+1,k+1}, \psi_h^{n+1,k} + \psi_{e,h}] = \psi_h^n\,. \end{cases} \tag{4.53}$$

This system is solved iteratively for each fixed time-step $n \in \mathbb{N}$ for the unknowns $(\phi_h^{n+1,k+1}, \psi_h^{n+1,k+1})$, $k \in \mathbb{N}$, starting from

$$\phi_h^{n+1,0} := \phi_h^n\,, \qquad \psi_h^{n+1,0} := \psi_h^n\,. \tag{4.54}$$

Again, to have uniqueness, one sets $\phi_{11}^{n+1,k+1} = 0$, for all $n, k \in \mathbb{N}$. The stopping criterion for the iterations in our simulations is

$$\frac{||\phi_h^{n+1,k+1} - \phi_h^{n+1,k}||_\infty}{||\phi_h^{n+1,k}||_\infty} + \frac{||\psi_h^{n+1,k+1} - \psi_h^{n+1,k}||_\infty}{||\psi_h^{n+1,k}||_\infty} < 10^{-2}\,. \tag{4.55}$$

A stricter stopping criterion does not significantly influence results, but leads to increased numerical cost. Supposing that the convergence criterion (4.55) has been reached after K steps, then the new solution at time-step $n+1$ is defined as

$$\phi_h^{n+1} := \phi_h^{n+1,K}\,, \qquad \psi_h^{n+1} := \psi_h^{n+1,K}\,. \tag{4.56}$$

Remark 4.5. ***(Convergence of fixed-point iterations.)*** *The particular linearization in Eq.* (4.53) *had the best convergence properties as compared to other linearizations tested. For example, in the tearing mode studies of Section 5, convergence was destroyed when replacing* $[\phi_h^{n+1,k}, \Delta\phi_h^{n+1,k}]$ *in the second line by* $[\phi_h^{n+1,k+1}, \Delta\phi_h^{n+1,k}]$ *or by* $[\phi_h^{n+1,k}, \Delta\phi_h^{n+1,k+1}]$. *Similarly, convergence has not been achieved when replacing* $[\psi_h^{n+1,k}, \Delta\psi_{e,h}]$ *by* $[\psi_h^{n+1,k+1}, \Delta\psi_{e,h}]$ *in the first equation of* (4.53) *and convergence is slower by about a factor two when replacing* $[\psi_h^{n+1,k+1}, \Delta\psi_{e,h}]$ *by* $[\psi_h^{n+1,k}, \Delta\psi_{e,h}]$. *Understanding the different convergence properties requires an in-depth study of the iteration functions (operators) arising from different linearizations, in particular a study of their spectrum. This is beyond the scope of this work.*

Furthermore, we implement a fully implicit Euler discretization of Eq. (4.44), i.e. the RMHD-model on the Alfvén time scale. The scheme is almost identical to (4.53), with the exception that ε appears at different positions and that the corresponding time-step is $\tau' = \tau/\sqrt{\varepsilon}$:

$$(\mathrm{ALF})_\varepsilon \begin{cases} (\mathbb{1} - \sqrt{\varepsilon}\tau'\Delta)\Delta\phi_h^{n+1,k+1} + \tau'[\Delta\psi_h^{n+1,k+1}, \psi_h^{n+1,k} + \psi_{e,h}] - \dfrac{\tau'}{2}[\psi_h^{n+1,k+1}, \Delta\psi_{e,h}] \\ \qquad\qquad = \Delta\phi_h^n - \tau'[\phi_h^{n+1,k}, \Delta\phi_h^{n+1,k}] + \dfrac{\tau'}{2}[\psi_h^{n+1,k}, \Delta\psi_{e,h}]\,, \\ (\mathbb{1} - \sqrt{\varepsilon}\tau'\Delta)\psi_h^{n+1,k+1} + \tau'[\phi_h^{n+1,k+1}, \psi_h^{n+1,k} + \psi_{e,h}] = \psi_h^n\,. \end{cases} \tag{4.57}$$

By means of these two implicit schemes, $(\mathrm{IMP})_\varepsilon$ and $(\mathrm{ALF})_\varepsilon$, we shall explore the behavior of solutions of the RMHD system in the two scalings (resistive as well as Alfvén time-scaling) in the HPF-limit (c.f. subsection 2.3). We shall see in Section 5 that the condition number of the discretization matrix A corresponding to the linear system (4.53) (accordingly scaled for $(\mathrm{ALF})_\varepsilon$) increases as ε tends to zero (as well as $\tau' \sim 1/\sqrt{\varepsilon}$ tends to infinity in $(\mathrm{ALF})_\varepsilon$). Below some critical value ε_c, which depends on the chosen space-time discretization meshes, the matrix A will become numerically singular, that is for $\varepsilon < \varepsilon_c$. This is an indication of the ill-posedness of the reduced model (2.21) in the continuous

regime. Hence the aim is to construct a scheme that overcomes this difficulty of standard schemes, in particular the numerical singularity for too small ε-values.

Let us remark here that a different fully implicit scheme has been introduced by Chacón et al. [9] for the resolution of the RMHD-model on the Alfvén time-scale, Eq. (2.18). We shall comment on the differences of the present work with respect to [9] in detail in subsection 4.5.

4.4. **The Micro-Macro scheme.** We shall now construct a scheme that overcomes the numerical singularity for $\varepsilon < \varepsilon_c$ observed in standard schemes. The new scheme is based on the considerations in Section 3, in particular on the reformulation (3.38).

Discretizing the reformulation (3.38) would indeed yield a scheme which behaves well in the limit $\varepsilon \to 0$. However, it is not yet clear how to compute and discretize in an efficient manner $\overline{\theta}^{\varepsilon} \in \mathcal{G}_{\psi^\varepsilon}$. The projection operator (A.74) is clearly intended for analytical purposes, but is not amenable to numerical calculations. To avoid this new difficulty, we shall develop further the reformulation and predetermine $\overline{\theta}^{\varepsilon} \in \mathcal{G}_{\psi^\varepsilon}$ via a second auxiliary variable χ^ε in a computationally more efficient way. Supposing that the part $(\theta^\varepsilon)^\star \in \mathcal{A}_{\psi^\varepsilon}$ is known, one can construct this second auxiliary variable $\chi^\varepsilon \in \mathcal{D}_\sharp$ by solving

$$\{\psi^\varepsilon, \chi^\varepsilon\} - \sigma' \Delta \chi^\varepsilon = \{\psi^\varepsilon, \theta^\varepsilon\}\,, \tag{4.58}$$

where the term $\sigma' \Delta \chi^\varepsilon$ is a stabilization term, needed to determine χ^ε uniquely. This technique is also used in [26]. If this stabilization is small enough (of the order of the truncation errors), equation (4.58) signifies that (up to truncation and round-off errors) $\chi^\varepsilon(t)_{|\mathcal{A}_{\psi^\varepsilon}} = \theta^\varepsilon(t)_{|\mathcal{A}_{\psi^\varepsilon}}$. Replacing now the term $\overline{\theta}^{\varepsilon}$ in (3.38) by $\theta^\varepsilon - \chi^\varepsilon$, a projection of this equation on $\mathcal{G}_{\psi^\varepsilon}$ permits to see that $\overline{\theta}^{\varepsilon}(t) = \overline{\chi}^{\varepsilon}(t)$. By this procedure, we fixed the value of $\theta^\varepsilon(t)$ on the level sets of $\psi^\varepsilon(t)$ via the auxiliary variable $\chi^\varepsilon(t)$.

Summarizing, this new reformulation of (3.23) reads

$$(RF2)_\varepsilon \begin{cases} \partial_t \Delta \phi^\varepsilon + \{\phi^\varepsilon, \Delta \phi^\varepsilon\} = \{\psi^\varepsilon, \theta^\varepsilon\} + \Delta^2 \phi^\varepsilon \\ \partial_t \psi^\varepsilon + \{\phi^\varepsilon, \psi^\varepsilon\} = \Delta \psi^\varepsilon - \Delta \psi_e \\ \{\psi^\varepsilon, \Delta \psi^\varepsilon\} = \varepsilon \{\psi^\varepsilon, \theta^\varepsilon\} - (\theta^\varepsilon - \chi^\varepsilon) \\ \{\psi^\varepsilon, \chi^\varepsilon\} - \sigma' \Delta \chi^\varepsilon = \{\psi^\varepsilon, \theta^\varepsilon\}\,. \end{cases} \tag{4.59}$$

Remark that the stabilization represents a systematic error, i.e. the system (4.59) is not equivalent to the system (3.38). In both sets of equations θ^ε is an auxiliary unknown, introduced to secure the well-posedness of the system for vanishing ε. The part of this function in $\mathcal{G}_\varepsilon$ being arbitrary, these two systems stem from different choices. We note,

however, that both systems will carry out equivalent numerical approximations of the physical quantities $(\phi^\varepsilon, \psi^\varepsilon)$, for all values of $\varepsilon \geq 0$, as soon as the stabilization error matches the truncation error of the scheme.

The next step is the implicit Euler discretization and the linearization of the reformulated problem (4.59), in a way to recover the correct asymptotics (3.36) in the limit $\varepsilon \to 0$. Let k again stand for the index of the fixed-point iteration during each time step $n \in \mathbb{N}$, then we linearize (4.59) as follows:

$$(RF_\tau)_\varepsilon \quad \begin{cases} (\mathbb{1} - \tau\Delta)\Delta\phi^{n+1,k+1} - \tau\{\psi^{n+1,k}, \theta^{n+1,k+1}\} = \Delta\phi^n - \tau\{\phi^{n+1,k}, \Delta\phi^{n+1,k}\} \\ (\mathbb{1} - \tau\Delta)\psi^{n+1,k+1} + \tau\{\phi^{n+1,k+1}, \psi^{n+1,k}\} = \psi^n - \Delta\psi_e \\ \{\psi^{n+1,k}, \Delta\psi^{n+1,k+1}\} = \varepsilon\{\psi^{n+1,k}, \theta^{n+1,k+1}\} - \beta'(\theta^{n+1,k+1} - \chi^{n+1,k+1}) \\ \{\psi^{n+1,k}, \chi^{n+1,k+1}\} - \sigma'\Delta\chi^{n+1,k+1} = \{\psi^{n+1,k}, \theta^{n+1,k+1}\}\,. \end{cases} \tag{4.60}$$

Here, we introduced a small parameter $\beta' \ll 1$ in the third equation, whose interest is to improve the properties of the system matrix when passing to the full discretization. This new parameter allows the use of increased values of the σ' parameter in the last equation of (4.60), which improves the conditioning of the system matrix, while keeping the influence of this stabilization negligible in the third equation.

Let us continue with the space discretization of (4.60). For this, we use the notation (4.50) and rewrite the problem in terms of the perturbations defined in Eq. (4.42), omitting the tildes in what follows. The fully-implicit micro-macro scheme reads

$$(\mathrm{MM})_\varepsilon \quad \begin{cases} (\mathbb{1} - \tau\Delta)\Delta\phi_h^{n+1,k+1} + \tau[\theta_h^{n+1,k+1}, \psi_h^{n+1,k} + \psi_{e,h}] = \Delta\phi_h^n - \tau[\phi_h^{n+1,k}, \Delta\phi_h^{n+1,k}]\,, \\ (\mathbb{1} - \tau\Delta)\psi_h^{n+1,k+1} + \tau[\phi_h^{n+1,k+1}, \psi_h^{n+1,k} + \psi_{e,h}] = \psi_h^n\,, \\ \varepsilon[\theta_h^{n+1,k+1}, \psi_h^{n+1,k} + \psi_{e,h}] + \beta'(\theta_h^{n+1,k+1} - \chi_h^{n+1,k+1}) - \dfrac{1}{\tau}[\psi_h^{n+1,k+1}, \psi_h^{n+1,k} + \psi_{e,h}] \\ \qquad - [[\phi_h^{n+1,k+1}, \psi_h^{n+1,k} + \psi_{e,h}], \psi_h^{n+1,k} + \psi_{e,h}] + \dfrac{1}{2}[\psi_h^{n+1,k+1}, \Delta\psi_{e,h}] \\ \qquad\qquad = -\dfrac{1}{\tau}[\psi_h^n, \psi_h^{n+1,k} + \psi_{e,h}] - \dfrac{1}{2}[\psi_h^{n+1,k}, \Delta\psi_{e,h}] \\ [\chi_h^{n+1,k+1}, \psi_h^{n+1,k} + \psi_{e,h}] + \sigma h^3\Delta\chi_h^{n+1,k+1} = [\theta_h^{n+1,k+1}, \psi_h^{n+1,k} + \psi_{e,h}]\,. \end{cases} \tag{4.61}$$

Remark that in the third equation we inserted $\Delta\psi_h^{n+1,k+1}$ from the second equation. This manipulation leads to better conditioning of the system matrix (by about two orders of magnitude) and to faster convergence in the fixed-point iteration. In the stabilization term in the fourth equation of (4.61) we set $\sigma' = \sigma h^3$, where $\sigma \ll 1$ is a small parameter and $h = \min(h_x, h_y)$ stands for the grid spacing. In order to have uniqueness of $\chi_h^{n+1,k+1}$ we fix $\chi_{11}^{n+1,k+1} = \theta_{11}^{n+1,k+1}$ at the point (x_1, y_1) (see Remark 4.4).

4.5. **A brief comparison with the work of Chacón et al. [9].** In order to put the current work into perspective, we compare some main features of the scheme $(\mathrm{MM})_\varepsilon$ given in Eq. (4.61) (see Eq. (B.82) in the Appendix for the second-order version) and of the fully-implicit, Alfvén time-scaled scheme developed in [9]. A summary is shown in Table 1. It can be seen that different methods, a priori of the same order, were used for time stepping as well as for space discretization of the hyperbolic terms. The non-linear Poisson brackets are treated with a fixed-point iteration in the current code whereas a Jacobian-free Newton method has been applied in [9]. In the latter, the algebraic matrix inversions are performed by means of an iterative Krylov method, whereas in the present work linear systems are solved directly by means of the MUMPS package [1, 2]. The main difference between the two codes is the treatment of the stiffness ($\varepsilon \ll 1$), arising in the HPF-limit, c.f. subsection 2.3. First of all, our code is based on a time-rescaling to the resistive time-scale, which is the natural time-scale to study the long-time dynamics of RMHD. As a result, the time step τ is fixed as $\varepsilon \to 0$. The stiffness is dealt with by reformulating the problem such that one obtains a non-singular scheme in the HPF-limit. The sophisticated preconditioning applied in [9] is certainly powerful for the values $\varepsilon = 10^{-6}$ and $\varepsilon = 10^{-8}$ tested in the publication. However, it seems inevitable that this scheme will become singular as the time step τ' (on the Alfvén time scale) tends to infinity. Our scheme avoids this singularity, albeit at the cost of additional computational complexity: the scheme $(\mathrm{MM})_\varepsilon$ features four unknowns, whereas the common RMHD codes feature two unknowns.

5. Simulation of magnetic island evolution

This part is devoted to the investigation of the numerical schemes[2] $(\mathrm{EXP})_\varepsilon$, $(\mathrm{IMP})_\varepsilon$, $(\mathrm{ALF})_\varepsilon$ and $(\mathrm{MM})_\varepsilon$ presented in Section 4. In particular, we shall focus on the growth of the magnetic islands in the so-called nonlinear tearing mode [5, 30]. Firstly, a brief introduction to the tearing mode physics is presented (Sec. 5.1). Analytical estimates of the island growth rate and size at saturation are precised in order to give some comparison results for the numerical experiments performed in the remainder of this section. In Sec. 5.2, we investigate the behavior of the presented schemes in both the short-time (Alfvén) regime

[2]All simulation results were obtained with the second order DIRK time-discretization schemes presented in Appendix B. The Euler schemes of Section 4 were used in the different stages of the DIRK schemes.

TABLE 1. Comparison of some main aspects of the scheme $(\mathrm{MM})_\varepsilon$ given in Eq. (4.61) and of the fully-implicit Alfvén time-scaled scheme of [9].

	scheme $(\mathrm{MM})_\varepsilon$, Eq. (4.61)	Chacón et al. [9]
Time stepping	DIRK, c.f. Remark 4.3 (second order)	Rannacher time stepping [29] (second order)
Hyperbolic terms	Arakawa discretization [3] (second order)	quadratic upstream int. QUICK [24] (second order)
Non-linearities	fixed-point iteration	Newton-Raphson method
Matrix inversion	direct: MUMPS [1, 2]	iterative: Jacobian-free Krylov
Stiffness ($\varepsilon \ll 1$)	micro-macro reformulation	preconditioning (as $\tau' \to \infty$)
Unknowns	$\widetilde{\phi}, \widetilde{\psi}, \theta, \chi$	ϕ, ψ
Time scale	resistive time τ_η	Alfvén time τ_A

and the long-time (resistive) regime of the tearing mode. The asymptotic parameter ε considered for these first experiments is varied in a range of intermediate values in order for the standard methods to provide reference solutions. Finally, Sec. 5.3 contains a comparison of the schemes $(\mathrm{IMP})_\varepsilon$, $(\mathrm{ALF})_\varepsilon$ and $(\mathrm{MM})_\varepsilon$ for vanishing ε-values in order to outline the advantages of the developed scheme $(\mathrm{MM})_\varepsilon$ in the HPF-limit as compared to standard implicit methods.

5.1. **The tearing mode.** Let us first specify the tearing mode configuration which precises the set up of the numerical experiment. The two dimensional computational domain $\Omega_p = [-L_x, L_x] \times [-L_y, L_y]$ is defined by

$$L_x = 2\pi\,, \qquad L_y = \frac{2\pi}{k}\,, \qquad 0 < k < 1\,, \tag{5.62}$$

with k a parameter referred to as the aspect ratio. The equilibrium state (ϕ_e, ψ_e) is chosen as

$$\phi_e = 0\,, \qquad \psi_e = -\cos(x)\,. \tag{5.63}$$

For the tearing mode to occur, it is essential that the magnetic field (derivative of the equilibrium flux function) is zero on the line $x = 0$, the so-called inversion line. The initial

condition for the perturbation to the equilibrium is defined as a small deviation of the flux function along the y-direction, precisely:

$$\widetilde{\phi}^{\varepsilon}(t=0)=0\,,\qquad \widetilde{\psi}^{\varepsilon}(t=0)=-\alpha\cos(ky)\,, \tag{5.64}$$

where $\alpha \ll 1$ denotes the strength of the perturbation. Moreover, the choice of an aspect ratio of the rectangular domain smaller than unity, hence $k<1$ and $L_y > L_x$, is a necessary condition for the island growth. In the subsequent examples a value of $k=0.91$ is used.

Figure 1 shows the island size evolution $w(t)$ computed thanks to the scheme $(\mathrm{IMP})_{\varepsilon}$, defined by Eq. (4.53), via [5,30]

$$w(t)=4|\widetilde{\psi}^{\varepsilon}(t,0,0)|^{1/2}\,, \tag{5.65}$$

on a space mesh with $N_x \times N_y = 512 \times 512$ points, a time step $\tau = 0.1$, a perturbation strength $\alpha = 10^{-6}$ and an asymptotic parameter $\varepsilon = 10^{-6}$. The final time is $T = 20$, which means that 20 resistive time units have been simulated, because the scheme $(\mathrm{IMP})_{\varepsilon}$ is scaled to the resistive time. Note that the ε-value used is rather large so that we can be confident with the numerical results provided by the implicit scheme. Three different stages can be observed:

(1) linear phase: the island size w grows exponentially at a rate γ: $w(t) \sim e^{\gamma t}$.
(2) nonlinear phase: the island size w grows linearly (Rutherford regime).
(3) saturation phase: the island size w approaches its steady-state value w_s.

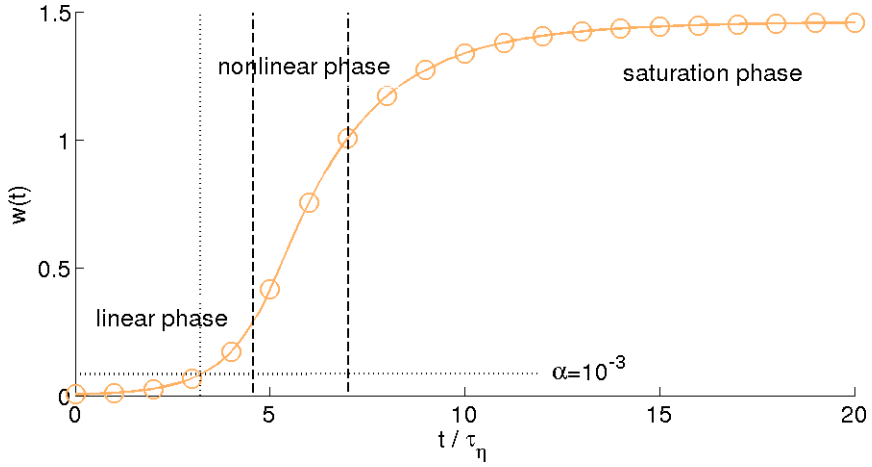

FIGURE 1. Simulated evolution of the island size $w(t)$ with $\alpha = 10^{-6}$ and $\varepsilon = 10^{-6}$. The three different growth phases, *i.e.* linear, nonlinear and saturation phase, are indicated. The value of the perturbation $\alpha = 10^{-3}$ used in the subsequent simulations is plotted in dotted lines.

The evolution of the vorticity $\Delta\phi_h^n$ and of the current density[3] $j_z = \Delta(\psi_h^n + \psi_e)$ for $\alpha = 10^{-3}$ is plotted in Figure 2. One observes the formation of a magnetic island with a symmetry axis at $x = 0$. The largest diameter of the island along the x-direction is located at $y = 0$ and is defined as the island size w whose evolution is discussed above. The border of the island is the so-called separatrix. The thickness of this separatrix, clearly visible in the plots of $\Delta\phi_h^n$, is the internal layer width δ. The points $(0, -\pi/k)$ and $(0, \pi/k)$, i.e. the end points of the separatrix, are the so-called X-points. The state shown at $t = 10$ is very close to the steady state.

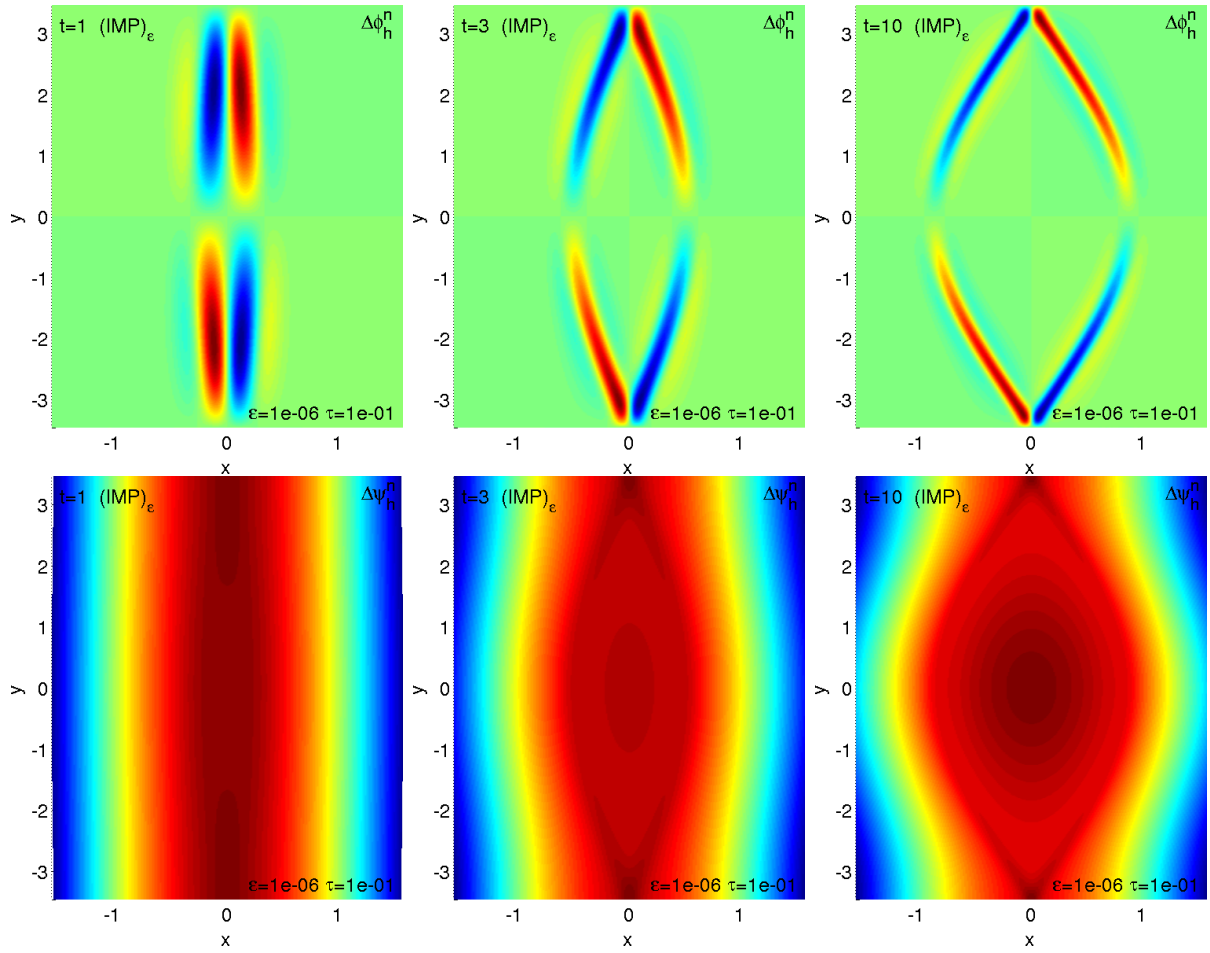

FIGURE 2. Simulation of the tearing mode for $\alpha = 10^{-3}$ and $\varepsilon = 10^{-6}$ with the scheme $(\mathrm{IMP})_\varepsilon$ with $\tau = 10^{-1}$ and $N_x \times N_y = 512 \times 512$.

[3]We remind the reader that the solutions obtained with the presented numerical schemes are the perturbations to the equilibrium $(\phi_e = 0, \psi_e = -\cos x)$, c.f. the notation (4.50).

In view of the validation of our numerical method, we wish to compare the results obtained by simulations with analytic estimates. Let us thus mention here some words about the parameters for which an analytic estimate can be computed thanks to theoretical developments.

The linear analysis of tearing modes was first developed by Furth et al. [16]. A key parameter of this theory is the stability parameter, denoted Δ', which can be understood as the jump in the logarithmic derivative of the flux function $\psi(x, y = 0)$ computed in $x = 0$ (see Refs. [15,16,25,28,30] for a precise definition). In the present case, the stability parameter is given by

$$\Delta' = 2\kappa \tan(\kappa\pi/2)\,, \tag{5.66}$$

where $\kappa = (1-k^2)^{1/2}$. For values of the product $\Delta'\delta \ll 1$, the so-called constant-ψ approximation can be made, with the following estimates (including viscosity in the equation for the stream function):

$$\delta \sim \varepsilon^{1/6} k^{-1/3}\,, \qquad \gamma \sim 1/\delta \sim \Delta' \varepsilon^{-1/6} k^{1/3}\,. \tag{5.67}$$

Figure 3 explains how the parameters Δ' and δ are computed from the numerical results, with the aim to check (5.67).

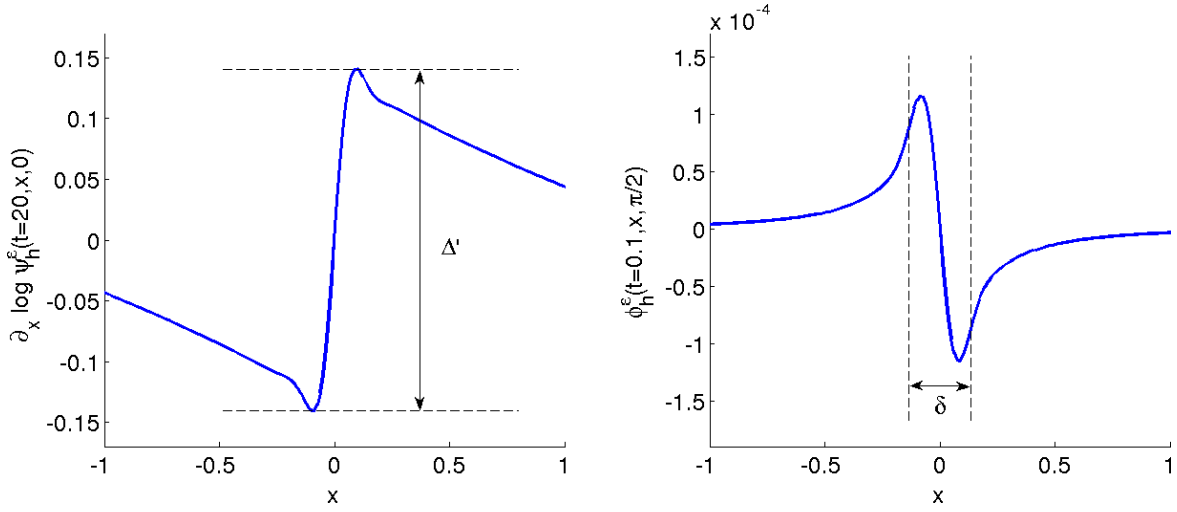

FIGURE 3. Tearing mode parameters Δ' (jump in logarithmic derivative) and δ (internal layer width). The layer width δ is determined in the linear phase at $t = 0.1$ and Δ' is determined close to the steady state.

In the nonlinear regime, the island width exceeds the resistive layer width and the condition of small Δ' becomes $\Delta' w \ll 1$, which must be satisfied for the Rutherford's

calculation [30] to be valid. The main result of Rutherford is the linear island growth (phase (2) on Figure 1) according to

$$w(t) = 1.22\Delta' t, \tag{5.68}$$

which is independent of ε (in units of Eq. (1.1)). This means that the nonlinear growth of the island occurs on the resistive time scale. Note also that, as the island grows, the condition $\Delta' w \ll 1$ may break down, leading to the switch to a different regime not covered by Rutherford's calculation, that does not extend to the tearing mode saturation (phase (3) on Figure 1). Analytic investigations of this regime are performed in the works Refs. [15, 25], yielding an estimate of w_s, the width of the island at saturation, given by

$$w_s = 2.44\Delta' . \tag{5.69}$$

Again, the validity of the calculations rely on the constant-ψ approximation, implying that at saturation the condition $\Delta'\delta \ll 1$ holds.

After having briefly described the behaviour of the solution $(\phi^\varepsilon, \psi^\varepsilon)$ of the (RMHD)-model (3.23) when considered in the tearing mode configuration (5.62)-(5.64), let us now come to the validation phase of the here presented numerical scheme.

5.2. **Validation of the $(\mathrm{MM})_\varepsilon$ scheme by comparisons with the $(\mathrm{EXP})_\varepsilon$, $(\mathrm{IMP})_\varepsilon$ and $(\mathrm{ALF})_\varepsilon$ schemes.** This section is devoted to the validation of the $(\mathrm{MM})_\varepsilon$ scheme (4.61) for the two different regimes considered so far: the fast plasma dynamics (on the Alfvén time scale) and the plasma dynamics on larger time scales (i.e. on the resistive time scale). With this aim, the computations carried out thanks to the $(\mathrm{MM})_\varepsilon$ scheme are compared to those obtained with the $(\mathrm{EXP})_\varepsilon$ (4.51), $(\mathrm{IMP})_\varepsilon$ (4.53) and $(\mathrm{ALF})_\varepsilon$ (4.57) schemes. The value of ε is chosen not to small in order to ensure, on the one hand, that the computational cost of the explicit discretization remains tractable, at least for the short time regime and, on the other hand, that implicit discretizations are able to provide reference solutions for the long-time regime. The set up is defined as follows: the asymptotic parameter is set to $\varepsilon = 10^{-6}$ and the strength of the initial perturbation is $\alpha = 10^{-3}$ for the remainder of this work. In the scheme $(\mathrm{MM})_\varepsilon$ the small stabilization parameters are $\beta' = \alpha h^3$ and $\sigma = \alpha$. For the short-time regime, the final simulation time is defined by $T = 0.2\,\tau_\eta$, while for the long-time regime this final time is set to $T = 10\,\tau_\eta$. The $(\mathrm{MM})_\varepsilon$ scheme simulation results will be compared to two reference solutions obtained as follows:

$$\text{short-time regime } (T = 0.2): \quad (\mathrm{EXP})_\varepsilon \text{ with } N_x \times N_y = 512 \times 512\,, \tau = 10^{-5} \tag{5.70}$$

$$\text{long-time regime } (T = 10): \quad (\mathrm{IMP})_\varepsilon \text{ with } N_x \times N_y = 512 \times 512\,, \tau = 10^{-1}\,. \tag{5.71}$$

Results for the short-time regime are summarized in Table 2. The indicated errors for both ϕ and ψ are the relative errors in max-norm with respect to the reference solution

(5.70) at the final time T. The consumed CPU times are relative to that of the computation performed with the $(\mathrm{IMP})_\varepsilon$ scheme on the 256×256 grid. The condition number estimated by MUMPS [1, 37] is denoted by $C1$. It is clearly observed that all four schemes approach

TABLE 2. Comparison of the four schemes $(\mathrm{EXP})_\varepsilon$, $(\mathrm{IMP})_\varepsilon$, $(\mathrm{ALF})_\varepsilon$ and $(\mathrm{MM})_\varepsilon$ for $\varepsilon = 10^{-6}$ ($S_L = 10^3$) in the short-time regime $T = 0.2\,\tau_\eta$.

scheme	$N_x \times N_y$	time step	$C1$	ϕ-error	ψ-error	$Rel.t_{CPU}$
$(\mathrm{EXP})_\varepsilon$	32×32	10^{-4}	10^3	1.98	0.33	13.6%
$(\mathrm{EXP})_\varepsilon$	64×64	10^{-4}	$7 \cdot 10^3$	0.49	0.09	50.8%
$(\mathrm{EXP})_\varepsilon$	128×128	10^{-4}	$3 \cdot 10^4$	0.18	0.03	193%
$(\mathrm{EXP})_\varepsilon$	256×256	$5 \cdot 10^{-5}$	10^5	0.08	0.01	1421%
$(\mathrm{IMP})_\varepsilon$	32×32	10^{-1}	10^6	1.96	0.33	1.9%
$(\mathrm{IMP})_\varepsilon$	64×64	10^{-1}	10^7	0.50	0.09	4.4%
$(\mathrm{IMP})_\varepsilon$	128×128	10^{-1}	10^8	0.19	0.03	19.3%
$(\mathrm{IMP})_\varepsilon$	256×256	10^{-1}	10^9	0.08	0.01	100%
$(\mathrm{ALF})_\varepsilon$	32×32	10^2	$3 \cdot 10^4$	1.96	0.33	2%
$(\mathrm{ALF})_\varepsilon$	64×64	10^2	$2 \cdot 10^5$	0.50	0.09	4.5%
$(\mathrm{ALF})_\varepsilon$	128×128	10^2	$2 \cdot 10^6$	0.19	0.03	23.5%
$(\mathrm{ALF})_\varepsilon$	256×256	10^2	10^7	0.08	0.01	95.1%
$(\mathrm{MM})_\varepsilon$	32×32	10^{-1}	$4 \cdot 10^6$	1.32	0.26	3.2%
$(\mathrm{MM})_\varepsilon$	64×64	10^{-1}	$8 \cdot 10^7$	0.49	0.09	11%
$(\mathrm{MM})_\varepsilon$	128×128	10^{-1}	10^9	0.19	0.03	56.7%
$(\mathrm{MM})_\varepsilon$	256×256	10^{-1}	$2 \cdot 10^{10}$	0.08	0.01	280%

the reference solution as the number of mesh points increases. However, the time step is not reduced along with the mesh interval, which explains that the second order accuracy of the schemes is not totally recovered in these results. The advantage of the implicit schemes as compared to the explicit one regarding the computational cost is evident. We shall point out that the fast Alfvén dynamics can be accurately resolved with implicit schemes, in particular with the scheme $(\mathrm{MM})_\varepsilon$, when the time step is adjusted accordingly. This is demonstrated in Figure 4, which was obtained thanks to the scheme $(\mathrm{MM})_\varepsilon$ with the two different time steps $\tau = 10^{-2}$ and $\tau = 10^{-3}$ on a space mesh with $N_x \times N_y = 128 \times 128$. A refined time step allows thus the tracking of the transient associated to the Alfvén dynamics via the $(\mathrm{MM})_\varepsilon$ scheme, however with an increased numerical damping (plots of the Figure 4 second line) as compared to the explicit scheme (first line of Figure 4). Note that this may be explained, at least partially, by the large time step and mesh interval used for the $(\mathrm{MM})_\varepsilon$ schemes compared to that of the explicit method. For the largest time step, the $(\mathrm{MM})_\varepsilon$ scheme jumps over the Alfvén wave dynamics to reach the formation of

the magnetic island (see the plots of the Figure 4 last line). Note that the approximations obtained at the final time are very similar, regardless of the time step and the numerical method.

Results for the long-time regime (nonlinear tearing mode dynamics) are summarized in Table 3. Two relative errors in max-norm are given with respect to the reference solution (5.71), namely the one left to the slash taken at the final time T and the one right to the slash which is the maximum error occurring over time. All implicit methods yield similar accuracy, the $(\mathrm{MM})_\varepsilon$ scheme being slower than the standard schemes, as expected, due to the increased number of unknowns. This drawback will be put into balance with the advantages presented in the following subsections and in particular with the capabilities of the $(\mathrm{MM})_\varepsilon$ for vanishing ε-values.

TABLE 3. Comparison of the three schemes $(\mathrm{IMP})_\varepsilon$, $(\mathrm{ALF})_\varepsilon$ and $(\mathrm{MM})_\varepsilon$ for $\varepsilon = 10^{-6}$ ($S_L = 10^3$) in the long-time regime $T = 10\,\tau_\eta$.

scheme	$N_x \times N_y$	time step	$C1$	ϕ-error	ψ-error	Rel. t_{CPU}
$(\mathrm{IMP})_\varepsilon$	32×32	10^{-1}	10^7	1.26/1.65	0.44/0.76	1.2%
$(\mathrm{IMP})_\varepsilon$	64×64	10^{-1}	10^8	0.34/0.40	0.12/0.18	4.4%
$(\mathrm{IMP})_\varepsilon$	128×128	10^{-1}	$9 \cdot 10^8$	0.11/0.14	0.04/0.05	21.2%
$(\mathrm{IMP})_\varepsilon$	256×256	10^{-1}	$7 \cdot 10^9$	0.03/0.04	0.01/0.01	100%
$(\mathrm{ALF})_\varepsilon$	32×32	10^2	$5 \cdot 10^4$	1.26/1.65	0.44/0.76	1.3%
$(\mathrm{ALF})_\varepsilon$	64×64	10^2	$4 \cdot 10^5$	0.34/0.40	0.12/0.18	4.5%
$(\mathrm{ALF})_\varepsilon$	128×128	10^2	$3 \cdot 10^6$	0.11/0.14	0.04/0.05	22.5%
$(\mathrm{ALF})_\varepsilon$	256×256	10^2	$2 \cdot 10^7$	0.03/0.04	0.01/0.01	83.1%
$(\mathrm{MM})_\varepsilon$	32×32	10^{-1}	$1 \cdot 10^6$	1.23/1.47	0.43/0.65	2.4%
$(\mathrm{MM})_\varepsilon$	64×64	10^{-1}	$2 \cdot 10^7$	0.34/0.40	0.12/0.18	12.5%
$(\mathrm{MM})_\varepsilon$	128×128	10^{-1}	$3 \cdot 10^8$	0.12/0.14	0.04/0.05	48.7%
$(\mathrm{MM})_\varepsilon$	256×256	10^{-1}	$5 \cdot 10^9$	0.03/0.04	0.01/0.01	265%

5.3. **Comparisons of the implicit schemes in the HPF-limit.** The actual goal of this work is the derivation of a scheme that overcomes the numerical singularity of standard schemes in the HPF-limit. Since the small-ε regime is intractable with explicit discretizations, we shall explore this limit with the three implicit schemes (4.53), (4.57) and (4.61). The objective here is twofold. Firstly, we aim to point out that the degeneracy of standard implicit schemes is overcome thanks to the micro-macro decomposition used to derive the $(\mathrm{MM})_\varepsilon$ scheme. Secondly, we wish to demonstrate that the computations carried out by this scheme are in good agreement with the analytic estimates regardless to ε-values.

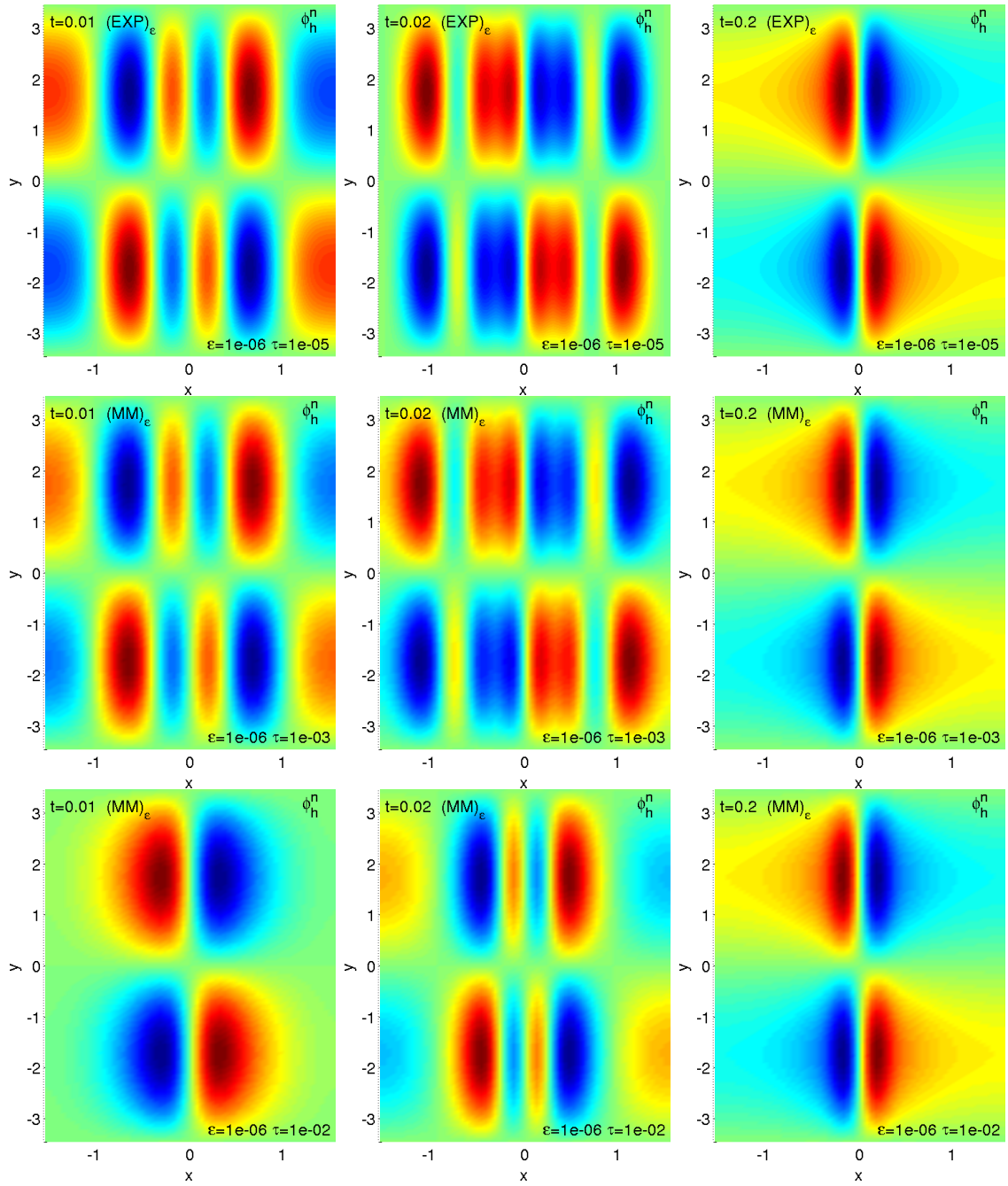

FIGURE 4. Simulated stream function ϕ_h^n obtained with the $(\mathrm{MM})_\varepsilon$ scheme with $\varepsilon = 10^{-6}$, time steps $\tau = 10^{-3}$ and $\tau = 10^{-2}$ at three different instances in time on a 128×128 mesh. The reference solution (5.70) computed on a 512×512 mesh with $\tau = 10^{-5}$ thanks to the explicit scheme is plotted on the first line.

The first numerical experiments are carried out on meshes with $N = 128$, $N = 256$ and $N = 512$ grid points in each direction and with a time step $\tau = 0.1$ equal to the final computational time $T = 0.1$ (equivalently $\tau' = \tau/\sqrt{\varepsilon} = T_A$ for the scheme $(\mathrm{ALF})_\varepsilon$). The chosen stabilization parameters in the scheme $(\mathrm{MM})_\varepsilon$ are $\beta' = \sqrt{\alpha}h^3$ and $\sigma = \sqrt{\alpha}$, where $\alpha = 10^{-3}$. The value of the time step is kept constant while the asymptotic parameter ε is decreased from 10^{-6} to 10^{-16}. The latter value corresponds to a Reynolds (and Lundquist) number expected to describe the fusion plasma in ITER. This is thus, the typical value of interest.

In Figure 5 we show the ε-dependence of the number of fixed-point iterations per time step and the condition number of the system matrix associated to the implicit discretizations. In the scheme $(\mathrm{IMP})_\varepsilon$ the condition number is inversely proportional to ε. A much better condition number is found for the scheme $(\mathrm{ALF})_\varepsilon$, proportional to $\varepsilon^{-1/2}$. As expected, the condition number for the scheme $(\mathrm{MM})_\varepsilon$ hardly depends on ε, one essential feature of the newly developed method.

A bad condition number translates to an increased number of fixed-point iterations per time step, as can be observed in the left panels of Figure 5. Note that the maximum number of iterations per time step was bounded to 100. In both the $(\mathrm{IMP})_\varepsilon$ and $(\mathrm{ALF})_\varepsilon$ schemes the loss of convergence of the fixed-point iteration for small ε reflects the expected numerical singularity in the HPF-limit. Remark also the difference between these two schemes. The $(\mathrm{ALF})_\varepsilon$ ceases to converge already at $\varepsilon = 10^{-10}$, which underlines somehow the fact that, for long time simulation, a change of the time-variable on the continuous level is preferable before discretization.

Summarizing, Figure 5 demonstrates that standard implicit schemes are numerically singular in the HPF-limit $\varepsilon \to 0$, whereas the micro-macro scheme $(\mathrm{MM})_\varepsilon$ keeps its numerical properties, independent of ε. In the sequel of this section we address the question of the $(\mathrm{MM})_\varepsilon$-validation in the HPF-limit. The experiments discussed above demonstrate that this validation cannot be obtained by comparisons with the outputs of the standard implicit discretizations. For this reason, the results obtained with the $(\mathrm{MM})_\varepsilon$ scheme are compared to the analytic estimates of the physical parameters introduced in section 5.1.

The numerical experiments are performed on a space-time grid with $N_x \times N_y = 128 \times 128$ and $\tau = 0.1$. The final simulation time is $T = 10$ and the stabilization parameters are $\beta' = \alpha h^3$ and $\sigma = \alpha$, where $\alpha = 10^{-3}$. The evolution of the island size $w(t)$ is depicted in Figure 6. We observe that, as ε gets smaller, the exponential growth phase gets "jumped" and one enters directly the non-linear phase, which is characterized by a linear growth and the subsequent saturation (see Figure 1). The simulation results depicted in Figure

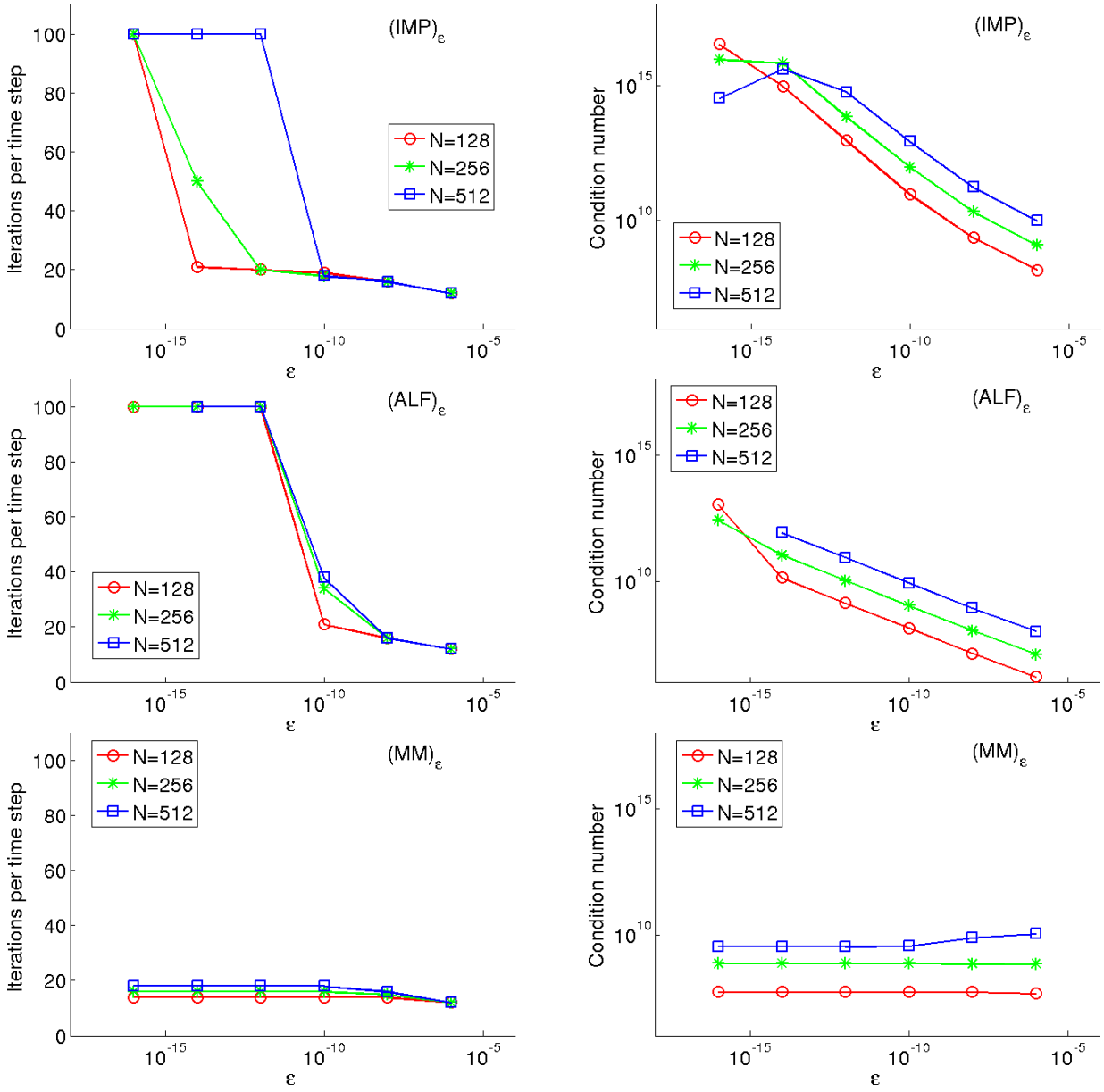

FIGURE 5. Number of fixed-point iterations per time step and condition number of the system matrix as functions of ε.

6 yield the following dependencies and parameters characterizing the island growth (to be compared with (5.67)-(5.69)):

$$\gamma \sim \varepsilon^{-1/4}\,, \quad \delta \sim \varepsilon^{1/6}\,, \quad \Delta' = 0.66\,, \quad \dot{w} = 0.84\Delta'\,, \quad w_s = 1.48 = 2.24\Delta'\,. \tag{5.72}$$

Note that the scaling of γ is obtained from exponential fits of the curves for intermediate values of the asymptotic parameter $10^{-7} \leq \varepsilon \leq 10^{-5}$, in order to secure a sufficient resolution in the linear regime (see Fig. 6). The parameters δ and Δ' are determined according to Figure 3 and all parameters of the nonlinear phase are obtained from the curve with $\varepsilon = 0$.

The agreement with the analytic theory for the island width at saturation is very good, considering also that the theory is valid for small islands, to the first order in the island width. The coefficient of the island growth in the nonlinear (Rutherford) phase is about 70% of the theoretical one. This is not too bad, considering that, to make the Rutherford regime evident, the island width must be much larger than the linear layer width but also much smaller than the saturation width. A better agreement would be expected by running at a higher resolution.

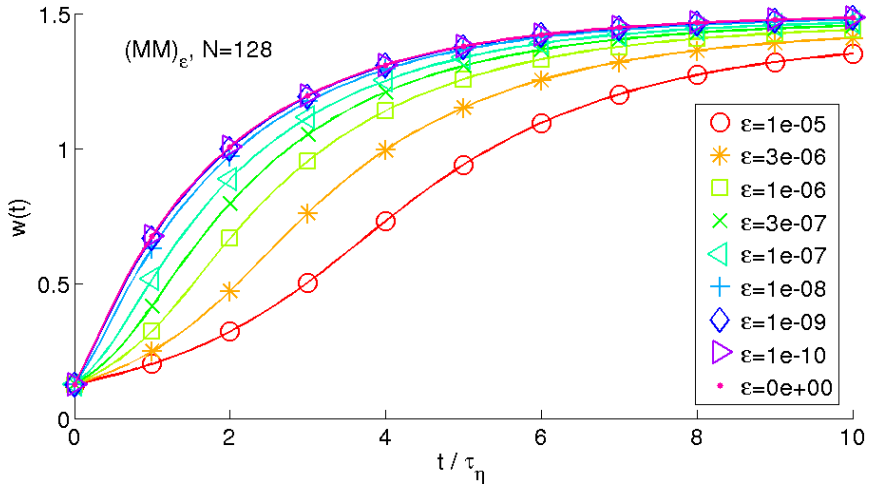

FIGURE 6. Simulated evolution of the island size $w(t)$ for different values of ε.

Indeed, a space grid with 128 points in each direction is not able to resolve the internal layer for the smallest ε-values. In order to capture accurately these gradients, one should resort to adaptive mesh techniques, which could be implemented together with the newly-developed micro-macro scheme. The possible benefit of such a combination is briefly demonstrated in Figure 7, where we compare the evolution of the stream function ϕ_h^ε at $\varepsilon = 0$ for two different space grids. The improvement of the internal layer resolution on the refined grid with $N_x \times N_y = 256 \times 256$ points is conclusive, with a significant reduction of the layer width as compared to that of the 128×128 mesh. Further mesh refinement would lead to even better resolution of the internal layer, however, the internal layer width δ is observed to have the right asymptotic behaviour ($\delta \sim \varepsilon^{-1/6}$) as long as the mesh resolution

is sufficient to capture the gradients. Moreover, the overall dynamics of the island formation (opening of the branches at the X-points) is well accounted for with the micro-macro scheme $(\mathrm{MM})_\varepsilon$, even on a coarse mesh and including the case $\varepsilon = 0$.

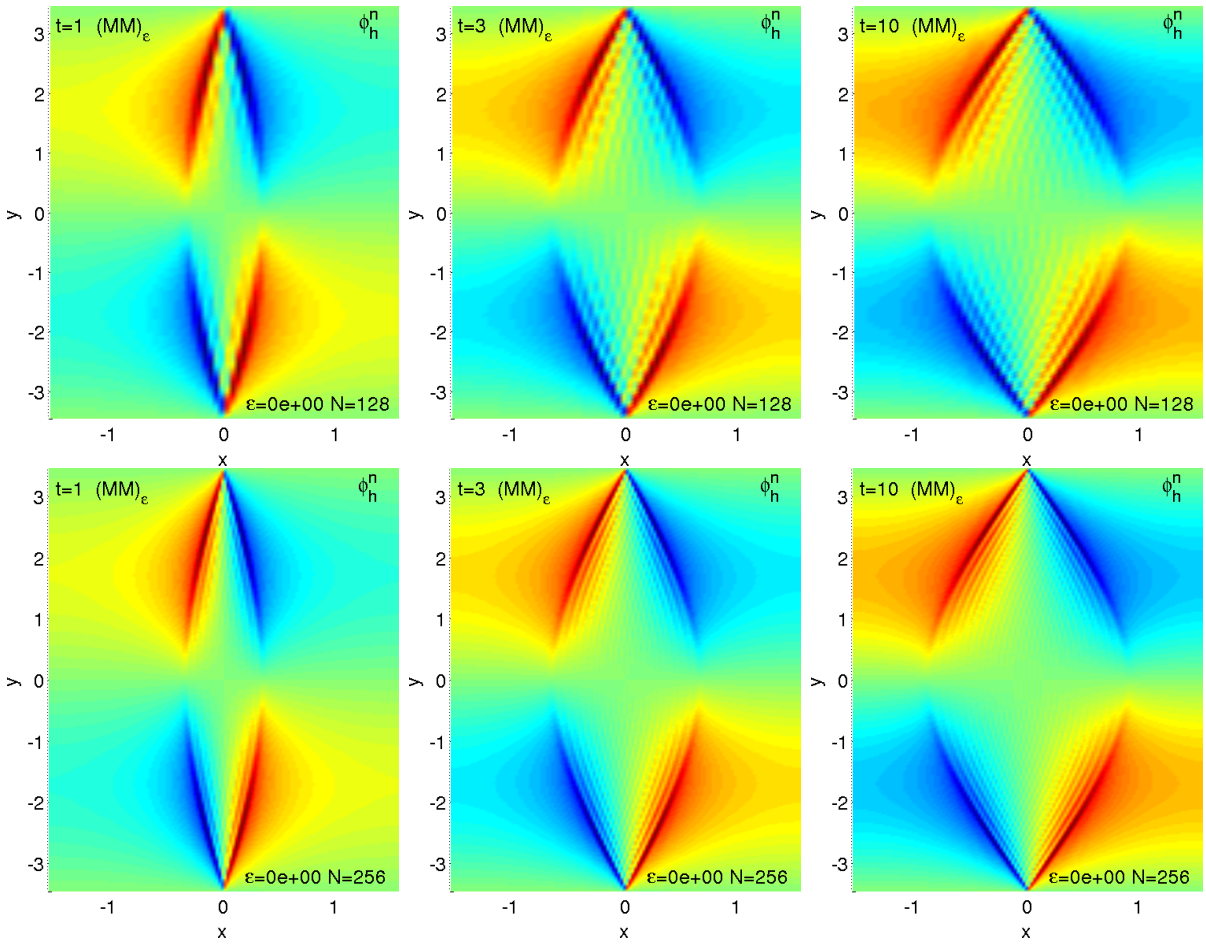

FIGURE 7. Simulated stream function ϕ_h^ε for $\varepsilon = 0$ obtained with the scheme $(\mathrm{MM})_\varepsilon$ on space grids with $N_x \times N_y = 128 \times 128$ and with $N_x \times N_y = 256 \times 256$ points, respectively.

Finally, this section is concluded by pointing out the weakness of standard implicit discretizations and their degeneracy for small ε-values. This is illustrated in Figure 8 displaying the stream function computed with the schemes $(\mathrm{IMP})_\varepsilon$ and $(\mathrm{MM})_\varepsilon$, for $\varepsilon = 10^{-14}$, plotted at time $t = 3$. Note that this value of the asymptotic parameter is two orders of magnitude above the values relevant for the ITER tokamak simulation. The stream function computed thanks to the standard implicit method is totally non-physical. Due to the singular nature of the HPF-limit, standard discretizations can not accurately account for the microscopic part of the vorticity equation (first equation of $(P)_\varepsilon$). This

is precisely where the micro-macro approach developed here brings a dramatic advantage over existing methods.

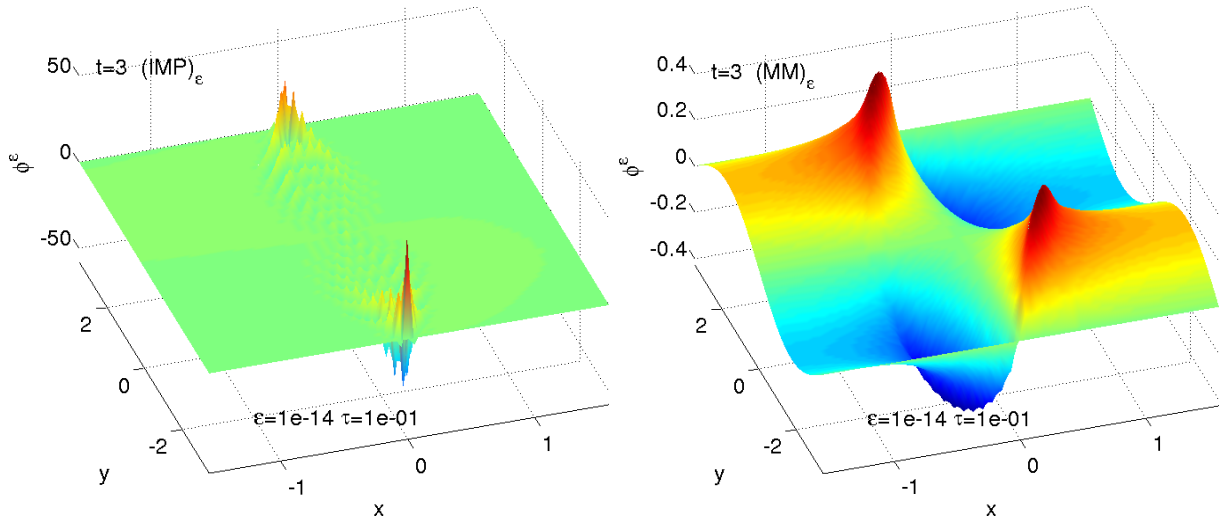

FIGURE 8. Simulated stream functions ϕ_h^n obtained with the schemes $(\mathrm{IMP})_\varepsilon$ and $(\mathrm{MM})_\varepsilon$, for $\varepsilon = 10^{-14}$, on a space mesh $N_x \times N_y = 128 \times 128$.

6. Conclusion

Magnetically-confined tokamak plasmas can be largely perturbed by instabilities, like the here investigated tearing modes, which can lead to the formation of magnetic islands and disruptive energy releases in the tokamak. We presented in this work an efficient numerical method for the resolution of the reduced resistive MHD model (RMHD), permitting the study of magnetic island formation as it pertains to linear and non-linear growth as well as to the saturation regime. In particular, our method was shown to allow the choice of large time steps, associated to the resistive dynamics, in the parameter range expected for large-scale tokamaks. The obtained results were shown to agree well with analytical estimates. A difficulty remains still to be handled within future works. Indeed, the creation of an internal layer requires the use of refined meshes in space. Adaptive grids or multiscale methods are some possibilities to cope with this problem.

Acknowledgements

We acknowledge the support of the "Agence Nationale de la Recherche" (ANR) in the frame of the contract BOOST (Building the future Of numerical methOdS for iTer) as well as of the FR-FCM (Fédération de Recherche pour la Fusion par Confinement Magnétique). Moreover, we thank J. Narski and A. Lozinski for fruitful discussions during the development of this work. This work was also supported by the European Communities under the

contract of Association between EURATOM and CEA. The views and opinions expressed herein do not necessarily reflect those of the European Commission.

A. Geometric interpretation of the Micro-Macro decomposition

In this part, the magnetic field $\mathbf{B}_p$ is assumed sufficiently smooth, satisfying $\mathbf{B}_p \neq 0$ in Ω, so that we can introduce the following directional field

$$\mathbf{b} := \mathbf{B}_p/|\mathbf{B}_p| = \mathbf{B}_p/|\nabla\psi|\,,$$

which is the unit tangent to the isolines of ψ, the unit normal being $\mathbf{n} := \frac{\nabla\psi}{|\nabla\psi|}$. The purpose is here to give, in this smooth framework, a geometrical interpretation of the abstract decomposition introduced in Section 3.1.

First, let us find an expression for the orthogonal projection operator P_ψ on the kernel of T_ψ, which is needed for the decomposition (3.33), in other words for the splitting of a function into its average and fluctuation parts. This projection operator is simply defined as the integration of a function along the field lines of $\mathbf{B}_p$. To introduce this operator, let us denote for fixed $(x_0, y_0) \in \Omega$ by $\gamma_{(x_0,y_0)} : [0, L_{(x_0,y_0)}] \to \Omega$ the solution of the ODE

$$\begin{cases} \gamma'(s) = \mathbf{b}(\gamma(s)) \quad \forall s \in [0, L_{(x_0,y_0)}] \\ \exists s_0 \in [0, L_{(x_0,y_0)}] \text{ such that } \gamma(s_0) = (x_0, y_0)\,, \end{cases} \tag{A.73}$$

which is a parametrized curve (by the arc length, unit speed), passing through (x_0, y_0), of length $L_{(x_0,y_0)}$ and describing the isolines of ψ, *i.e.* the level sets $C_t := \{(x, y) \in \Omega \,/\, \psi(x, y) = t\}$. Remark that all the level sets can be considered as closed, due to periodicity reasons. This means that $\gamma_{(x_0,y_0)}(0) = \gamma_{(x_0,y_0)}(L_{(x_0,y_0)})$ and, while $s \in [0, L_{(x_0,y_0)}]$, the curve has been traveled only one time. One can now define the projection operator

$$P_\psi : \mathcal{D}_\sharp \to \mathcal{G}_\psi\,, \quad P_\psi(\phi)(x, y) := \frac{\int_0^{L_{(x,y)}} \frac{\phi}{|\nabla\psi|}(\gamma_{(x,y)}(s))\,ds}{\int_0^{L_{(x,y)}} \frac{1}{|\nabla\psi|}(\gamma_{(x,y)}(s))\,ds}, \tag{A.74}$$

and the kernel of this operator is nothing else than $\ker P_\psi = \mathcal{A}_\psi$, which can be rewritten as

$$\mathcal{A}_\psi := \{f \in \mathcal{D}_\sharp \,/\, \int_{C_t} \frac{f}{|\nabla\psi|}(\gamma_{(x,y)}(s))ds = 0 \quad \text{on any isoline } C_t \text{ of } \psi\}\,, \tag{A.75}$$

and corresponds to the set of functions with zero average along the field lines. Indeed, take any $f \in \mathcal{A}_\psi$ and any number t_0 in the image of ψ. Consider an isoline C_{t_0} corresponding to t_0 as well as the neighboring isolines C_t for $t \in (t_0 - \delta, t_0 + \delta)$ with some $\delta > 0$. Denote the domain formed by these isolines by N_δ. Provided δ is chosen small enough, we can assume that N_δ is a doubly connected subdomain (a domain with a single hole) of Ω that can be parametrized by (t, s), where the coordinate $t \in (t_0 - \delta, t_0 + \delta)$ "counts" the isolines, i.e. $t = \psi(x, y)$, and the coordinate $s \in (0, L_t)$ measures the arc length along each isoline

in N_δ, L_t being the length of the isoline C_t. We have then the following relations between the differentials of the new coordinates (t,s) and those of the old ones (x,y)

$$\begin{aligned} dt &= \partial_x\psi\, dx + \partial_y\psi\, dy \\ ds &= \frac{1}{|\nabla\psi|}\left(-\partial_y\psi\, dx + \partial_x\psi\, dy\right) . \end{aligned}$$

The first is just the differential of $t = \psi(x,y)$. The second expresses the fact that the isolines are perpendicular to $\nabla\psi$ and ds is the element of length of an isoline. We can now compute the Jacobian for the passage from (t,s) to (x,y):

$$\frac{\partial(t,s)}{\partial(x,y)} = \frac{1}{|\nabla\psi|}\begin{vmatrix} \partial_x\psi & \partial_y\psi \\ -\partial_y\psi & \partial_x\psi \end{vmatrix} = |\nabla\psi| .$$

Taking any function $g \in \mathcal{C}_c^\infty(t_0-\delta, t_0+\delta)$, we observe that $g\circ\psi \in \mathcal{G}_\psi$, so that for any $f \in \mathcal{A}_\psi$, one has

$$\begin{aligned} 0 = \int_\Omega (g\circ\psi) f\, dxdy = \int_{N_\delta} (g\circ\psi) f\, dxdy &= \int_{t_0-\delta}^{t_0+\delta}\int_0^{L_t} (g\circ\psi) f \frac{1}{|\nabla\psi|} ds\, dt \\ &= \int_{t_0-\delta}^{t_0+\delta} g(t)\left(\int_0^{L_t} \frac{f}{|\nabla\psi|} ds\right) dt. \end{aligned}$$

This implies (A.75) for all $t \in (t_0-\delta, t_0+\delta)$ since g is arbitrary. Reversing this argument, we easily prove that any f satisfying (A.75) is in $\mathcal{A}_\psi$.

Finally, let us also study in more details the problem of finding (for fixed $\psi \in W^{2,\infty}_\sharp$) the solution $\phi \in \mathcal{A}_\psi$ of

$$T_\psi(\phi) = \{\psi, \phi\} = f , \tag{A.76}$$

where $f \in \tilde{\mathcal{A}}_\psi$ is given. We have seen earlier that uniqueness can only be achieved by requiring $\phi \in \mathcal{A}_\psi$ and that the condition $f \in \tilde{\mathcal{A}}_\psi$ is necessary for solvability. In the case of smooth $\mathbf{B}_p \neq 0$ we can construct explicitly the solution of (A.76) by remarking that

$$\{\psi,\phi\} = f \;\Leftrightarrow\; \mathbf{B}_p\cdot\nabla\phi = f \;\Leftrightarrow\; \mathbf{b}\cdot\nabla\phi = \frac{f}{|\nabla\psi|} .$$

Using again the parametrization (A.73) of the isolines of ψ, one gets

$$\frac{d}{ds}\left(\phi(\gamma(s))\right) = \mathbf{b}(\gamma(s))\cdot\nabla\phi(\gamma(s)) = \frac{f}{|\nabla\psi|}(\gamma(s)) .$$

Integrating now this equation along an isoline, yields

$$\phi(\gamma(s)) = \phi(\gamma(0)) + \int_0^s \frac{f}{|\nabla\psi|}(\gamma(\sigma))d\sigma ,$$

which gives the solution of (A.76). Hence the problem (A.76) can be solved by simply integrating along the level sets of ψ. Note that $\phi(\gamma(0))$ can be arbitrarily chosen so that

the solution is unique modulo additive constants per isoline of ψ. This again underlines the fact that the solution ϕ of (A.76) can be only uniquely determined in $\mathcal{A}_\psi$.

B. The diagonally-implicit Runge-Kutta (DIRK) schemes

The implicit schemes presented in sections 4.3 and 4.4 have been elevated to second-order accuracy in time by means of the DIRK method (c.f. Remark 4.3). Generally, Runge-Kutta methods with $s > 1$ stages are characterized by a Butcher table,

$$\begin{array}{c|ccc} c_1 & a_{11} & \dots & a_{1s} \\ \vdots & \vdots & & \vdots \\ c_s & a_{s1} & \dots & a_{ss} \\ \hline & b_1 & \dots & b_s. \end{array} \tag{B.77}$$

A problem of the form $\partial_t u = G(u) + f(t)$, with G some (non)-linear operator and f a source-term, is thus discretized as follows: Let u^n stand for an approximation of $u(t_n)$ at $t_n = n\tau$, then u^{n+1} is determined via some intermediate steps u_i for $i = 1, \cdots, s$

$$\begin{aligned} u_i &= u^n + \tau \sum_{j=1}^{s} a_{ij}(G(u_j) + f(t + c_j\tau)) \\ u^{n+1} &= u^n + \tau \sum_{j=1}^{s} b_j(G(u_j) + f(t + c_j\tau)) \,. \end{aligned} \tag{B.78}$$

We remark that if $a_{s,j} = b_j$ for all $j = 1, \dots s$, then one has $u_s = u^{n+1}$. The DIRK method employed in this work is characterized by the following Butcher table:

$$\begin{array}{c|cc} \lambda & \lambda & 0 \\ 1 & 1-\lambda & \lambda \\ \hline & 1-\lambda & \lambda \end{array} \tag{B.79}$$

where $\lambda = 1 - 1/\sqrt{2}$. Within our DIRK schemes, the solutions u_h^{n+1} of the RMHD systems given in Eq. (4.43), in Eq. (4.44) on the Alfvén time scale or in Eq. (3.38) after reformulation, respectively, are obtained by means of two intermediate solutions, denoted by u_h^* and by u_h^{**}, respectively. The following two pages contain the DIRK versions of the first-order schemes (4.53), (4.57) and (4.61). Remark that at each stage of a DIRK algorithm, linearization and subsequent fixed-point iteration are carried out in exactly the same manner as in the first-order schemes.

DIRK version of the scheme $(\mathrm{IMP})_\varepsilon$ presented in (4.53):

$$
(\mathrm{IMP})_\varepsilon \begin{cases}
\text{Stage 1 :} \\
\varepsilon(\mathbb{1} - \lambda\tau\Delta)\Delta\phi_h^* + \lambda\tau\Big(\varepsilon[\phi_h^*, \Delta\phi_h^*] + [\Delta\psi_h^*, \psi_h^* + \psi_{e,h}] - [\psi_h^*, \Delta\psi_{e,h}]\Big) \\
\qquad\qquad = \varepsilon\Delta\phi_h^n \,, \\
(\mathbb{1} - \lambda\tau\Delta)\psi_h^* + \lambda\tau[\phi_h^*, \psi_h^* + \psi_{e,h}] = \psi_h^n \,. \\
\text{Stage 2 :} \\
\varepsilon(\mathbb{1} - \lambda\tau\Delta)\Delta\phi_h^{**} + \lambda\tau\Big(\varepsilon[\phi_h^{**}, \Delta\phi_h^{**}] + [\Delta\psi_h^{**}, \psi_h^{**} + \psi_{e,h}] - [\psi_h^{**}, \Delta\psi_{e,h}]\Big) \\
\qquad\qquad = \varepsilon\Delta\phi_h^n + \varepsilon\dfrac{1-\lambda}{\lambda}\left(\Delta\phi_h^* - \Delta\phi_h^n\right) \,, \\
(\mathbb{1} - \lambda\tau\Delta)\psi_h^{**} + \lambda\tau[\phi_h^{**}, \psi_h^{**} + \psi_e] = \psi_h^n + \dfrac{1-\lambda}{\lambda}\left(\psi_h^* - \psi_h^n\right) \,. \\
\text{Final result :} \\
(\phi_h^{n+1}, \psi_h^{n+1}) = (\phi_h^{**}, \psi_h^{**}) \,.
\end{cases}
\tag{B.80}
$$

DIRK version of the scheme $(\mathrm{ALF})_\varepsilon$ presented in (4.57):

$$
(\mathrm{ALF})_\varepsilon \begin{cases}
\text{Stage 1 :} \\
(\mathbb{1} - \sqrt{\varepsilon}\lambda\tau'\Delta)\Delta\phi_h^* + \lambda\tau'\Big([\phi_h^*, \Delta\phi_h^*] + [\Delta\psi_h^*, \psi_h^* + \psi_{e,h}] - [\psi_h^*, \Delta\psi_{e,h}]\Big) \\
\qquad\qquad = \Delta\phi_h^n \,, \\
(\mathbb{1} - \sqrt{\varepsilon}\lambda\tau'\Delta)\psi_h^* + \lambda\tau'[\phi_h^*, \psi_h^* + \psi_{e,h}] = \psi_h^n \,. \\
\text{Stage 2 :} \\
(\mathbb{1} - \sqrt{\varepsilon}\lambda\tau'\Delta)\Delta\phi_h^{**} + \lambda\tau'\Big([\phi_h^{**}, \Delta\phi_h^{**}] + [\Delta\psi_h^{**}, \psi_h^{**} + \psi_{e,h}] - [\psi_h^{**}, \Delta\psi_{e,h}]\Big) \\
\qquad\qquad = \Delta\phi_h^n + \dfrac{1-\lambda}{\lambda}\left(\Delta\phi_h^* - \Delta\phi_h^n\right) \,, \\
(\mathbb{1} - \sqrt{\varepsilon}\lambda\tau'\Delta)\psi_h^{**} + \lambda\tau'[\phi_h^{**}, \psi_h^{**} + \psi_e] = \psi_h^n + \dfrac{1-\lambda}{\lambda}\left(\psi_h^* - \psi_h^n\right) \,. \\
\text{Final result :} \\
(\phi_h^{n+1}, \psi_h^{n+1}) = (\phi_h^{**}, \psi_h^{**}) \,.
\end{cases}
\tag{B.81}
$$

DIRK version of the scheme $(\mathrm{MM})_\varepsilon$ presented in (4.61):

$$
(\mathrm{MM})_\varepsilon \quad \left\{ \begin{array}{l}
\text{Stage } 1 : \\
(\mathbb{1} - \lambda\tau\Delta)\Delta\phi_h^* + \lambda\tau\Big([\phi_h^*, \Delta\phi_h^*] + [\theta_h^*, \psi_h^* + \psi_{e,h}]\Big) = \Delta\phi_h^n \,, \\
(\mathbb{1} - \lambda\tau\Delta)\psi_h^* + \lambda\tau[\phi_h^*, \psi_h^* + \psi_{e,h}] = \psi_h^n \,, \\
[\theta_h^*, \psi_h^* + \psi_{e,h}] + \beta'(\theta_h^* - \chi_h^*) - [[\phi_h^*, \psi_h^* + \psi_{e,h}], \psi_h^* + \psi_{e,h}] \\
\qquad - \dfrac{1}{\lambda\tau}[\psi_h^*, \psi_h^* + \psi_{e,h}] + \dfrac{1}{2}[\psi_h^*, \Delta\psi_{e,h}] \\
\qquad\qquad = -\dfrac{1}{\lambda\tau}[\psi_h^n, \psi_h^* + \psi_{e,h}] - \dfrac{1}{2}[\psi_h^*, \Delta\psi_{e,h}] \,, \\
[\chi_h^*, \psi_h^* + \psi_{e,h}] + \sigma h^3 \Delta\chi_h^* = [\theta_h^*, \psi_h^* + \psi_{e,h}] \,. \\
\\
\text{Stage } 2 : \\
(\mathbb{1} - \lambda\tau\Delta)\Delta\phi_h^{**} + \lambda\tau\Big([\phi_h^{**}, \Delta\phi_h^{**}] + [\theta_h^{**}, \psi_h^{**} + \psi_{e,h}]\Big) = \Delta\phi_h^n + \dfrac{1-\lambda}{\lambda}(\Delta\phi_h^* - \Delta\phi_h^n) \,, \\
(\mathbb{1} - \lambda\tau\Delta)\psi_h^{**} + \lambda\tau[\phi_h^{**}, \psi_h^{**} + \psi_{e,h}] = \psi_h^n + \dfrac{1-\lambda}{\lambda}(\psi_h^* - \psi_h^n) \,, \\
[\theta_h^{**}, \psi_h^{**} + \psi_{e,h}] + \beta'(\theta_h^{**} - \chi_h^{**}) - [[\phi_h^{**}, \psi_h^{**} + \psi_{e,h}], \psi_h^{**} + \psi_{e,h}] \\
\qquad - \dfrac{1}{\lambda\tau}[\psi_h^{**}, \psi_h^{**} + \psi_{e,h}] + \dfrac{1}{2}[\psi_h^{**}, \Delta\psi_{e,h}] \\
\qquad\qquad = -\dfrac{1}{\lambda\tau}[\psi_h^n, \psi_h^{**} + \psi_{e,h}] - \dfrac{1}{2}[\psi_h^{**}, \Delta\psi_{e,h}] + \dfrac{1-\lambda}{\lambda^2\tau}[\psi_h^{**} + \psi_{e,h}, \psi_h^* - \psi_h^n] \,, \\
[\chi_h^{**}, \psi_h^{**} + \psi_{e,h}] + \sigma h^3 \Delta\chi_h^{**} = [\theta_h^{**}, \psi_h^{**} + \psi_{e,h}] \,. \\
\\
\text{Final result} : \\
(\phi_h^{n+1}, \psi_h^{n+1}, \theta_h^{n+1}, \chi_h^{n+1}) = (\phi_h^{**}, \psi_h^{**}, \theta_h^{**}, \chi_h^{**}) \,.
\end{array} \right. \tag{B.82}
$$

References

[1] P. R. Amestoy, I. S. Duff and J.-Y. L'Excellent, *Multifrontal parallel distributed symmetric and unsymmetric solvers*, Comput. Methods in Appl. Mech. Eng., **184** (2000) 501-520.

[2] P. R. Amestoy, I. S. Duff, J. Koster and J.-Y. L'Excellent, *A fully asynchronous multifrontal solver using distributed dynamic scheduling*, SIAM Journal of Matrix Analysis and Applications **23**(1) (2001) 1541.

[3] A. Arakawa, *Computational design for long-term numerical integration of the equations of fluid motion: two-dimensional incompressible flow. Part I*, Journal of Computational Physics **135** (1997) 103–114.

[4] R. J. Bickerton, J. W. Connor and J. B. Taylor, *Diffusion driven plasma currents and bootstrap tokamak*, Nature **229** (1971) 110-112.

[5] D. Biskamp, *Nonlinear Magnetohydrodynamics*, Cambridge University Press (1997).

[6] D. Biskamp, *Magnetic Reconnection in Plasmas*, Cambridge University Press (2000).

[7] S. I. Braginskii, *Transport processes in a plasma*, Reviews of plasma physics **1** (1965) 205.

[8] J.C. Butcher, *Numerical Methods for Ordinary Differential Equations*, John Wiley & Sons, Ltd. (2008).

[9] L. Chacón, D. A. Knoll and J. M. Finn, *An implicit, nonlinear reduced resistive MHD solver*, Journal of Computational Physics **178**(1) (2002) 15-36.

[10] Z. Chang et al., *Observation of Nonlinear Neoclassical Pressure-Gradient-Driven Tearing Modes in TFTR*, Physical review letters **74**(23) (1995) 4663.

[11] P. Degond, *Asymptotic-preserving schemes for fluid models of plasmas*, arXiv preprint arXiv:1104.1869 (2011).

[12] P. Degond, F. Deluzet, A. Lozinski, J. Narski, C. Negulescu, *Duality based Asymptotic-Preserving Method for highly anisotropic diffusion equations*, CMS (Communications in Math Sciences) **10** (2012), no. 1, 1–31.

[13] P. Degond, F. Deluzet, C. Negulescu, *An asymptotic preserving scheme for strongly anisotropic elliptic problems*, SIAM-MMS (Multiscale Modeling and Simulation) **8** (2010), no. 2, 645–666.

[14] P. Degond, A. Lozinski, J. Narski, C. Negulescu, *An asymptotic-preserving method for highly anisotropic elliptic equations based on a MicroMacro decomposition*, Journal of Computational Physics **231** (2012) 2724–2740.

[15] D. F. Escande and M. Ottaviani, *Simple and rigorous solution for the nonlinear tearing mode*, Physics Letters A **323**(3) (2004) 278-284.

[16] H. P. Furth, J. Killeen and M. N. Rosenbluth, *Finite-resistivity instabilities of a sheet pinch*, Physics of Fluids **6**(4) (1963) 459.

[17] D. S. Harned and D. D. Schnack, *Semi-implicit method for long time scale magneto-hydrodynamic computations in three dimensions*, Journal of Computational Physics **65**(1) (1986) 57-70.

[18] A. Hujeirat, *IRMHD: an implicit radiative and magneto-hydrodynamical solver for selfgravitating systems*, Monthly Notices of the Royal Astronomical Society **298**(1) (1998) 310-320.

[19] J.D. Jackson, *Classical Electrodynamics*, John Wiley & Sons (1999).

[20] S. Jin, *Efficient asymptotic-preserving (AP) schemes for some multiscale kinetic equations*, SIAM Journal on Scientific Computing **21**(2) (1999) 441-454.

[21] O. S. Jones, U. Shumlak and D. S. Eberhardt, *An implicit scheme for nonideal magnetohydrodynamics*, Journal of Computational Physics **130**(2) (1997) 231-242.

[22] B. B. Kadomtsev, *Collective phenomena in plasma*, Sov J. Plasma Phys. **1** (1976) 389.

[23] L. L. Lao and T. H. Jensen, *Magnetohydrodynamic equilibria of attached plasmas after loss of vertical stability in elongated tokamaks*, Nuclear fusion **31**(10) (1991) 1909.
[24] B. P. Leonard, *A stable and accurate convective modelling procedure based on quadratic upstream interpolation*, Computer methods in applied mechanics and engineering **19**(1) (1979) 59-98.
[25] F. Militello and F. Porcelli, *Simple analysis of the nonlinear saturation of the tearing mode*, Physics of Plasmas **11**(5) (2004) L13-L16.
[26] J. Narski and M. Ottaviani, *Asymptotic Preserving scheme for strongly anisotropic parabolic equations for arbitrary anisotropy direction*, submitted.
[27] C. Negulescu, *Asymptotic-Preserving schemes. Modeling, simulation and mathematical analysis of magnetically confind plasmas*, Riv. Mat. Univ. Parma. **4**(2) (2013) 265–343.
[28] M. Ottaviani and F. Porcelli. *Nonlinear collisionless magnetic reconnection*, Physical review letters **71**(23) (1993) 3802-3805.
[29] R. Rannacher, *Finite element solution of diffusion problems with irregular data*, Numerische Mathematik **43**(2) (1984) 309-327.
[30] P. H. Rutherford, *Nonlinear growth of the tearing mode*, Physics of Fluids **16** (1973) 1903.
[31] V. D. Shafranov, *Magneto-vortex rings*, Soviet Phys. JETP **6** (1958).
[32] B. Sportisse, *An analysis of operator splitting techniques in the stiff case*, Journal of Computational Physics **161** (2000) 140–168.
[33] H. R. Strauss, *Nonlinear, threedimensional magneto-hydrodynamics of noncircular tokamaks*, Physics of Fluids **19** (1976) 134.
[34] A. Sykes and J. A. Wesson. *Relaxation instability in tokamaks*, Physical Review Letters **37** (1976) 140-143.
[35] F. L. Waelbroeck, *Onset of the sawtooth crash*, Physical review letters **70** (1993) 3259-3262.
[36] A. A. Ware, *Pinch effect for trapped particles in a tokamak*, Physical Review Letters **25**(1) (1970) 15.
[37] weblink: *http://graal.ens-lyon.fr/MUMPS/doc/userguide_4.10.0.pdf*

† Institut de Mathématiques de Toulouse (UMR 5219), Université Paul Sabatier, 118 route de Narbonne, 31062 Toulouse Cedex 9, France

* Commissariat à l'énergie atomique et aux énergies alternatives (CEA), IRFM, F-13108 Saint-Paul-lez-Durance, France

E-mail address: fabrice.deluzet@math.univ-toulouse.fr
E-mail address: claudia.negulescu@math.univ-toulouse.fr
E-mail address: Maurizio.Ottaviani@cea.fr
E-mail address: stefan.possanner@math.univ-toulouse.fr